

# Density Functional Theory Study of Alkaline Earth-Based Titanate Perovskite Oxides: Unraveling Their Significance for Solar Cell Applications

Shirzad Jouybar, Leila Naji,\* Saeedeh Sarabadani Tafreshi,\* Sayed Ahmad Mozaffari, and Nora H. de Leuw\*

 Cite This: <https://doi.org/10.1021/acs.jpcc.4c03863>

 Read Online

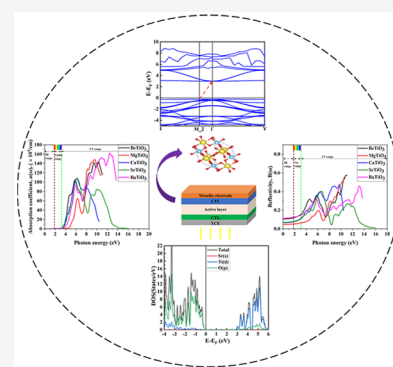
ACCESS |

 Metrics & More

 Article Recommendations

 Supporting Information

**ABSTRACT:** Charge transport layers (CTLs) and transparent conductive electrodes (TCEs) are important constituents of polymer solar cells (PSCs) and perovskite solar cells (Per-SCs), affecting the efficiency and stability of these devices. We employed density functional theory to study the structural, optoelectronic, thermal, and elastic properties of alkaline earth-based titanate perovskite oxides to determine the appropriate compounds for PSCs and Per-SCs. Based on the calculations,  $\text{CaTiO}_3$  exhibits a direct band gap of 3.535 eV, while  $\text{BeTiO}_3$ ,  $\text{MgTiO}_3$ ,  $\text{SrTiO}_3$ , and  $\text{BaTiO}_3$  displayed indirect band gap energies of 3.618, 4.852, 3.193, and 2.960 eV, respectively. Considering the calculated valence and conduction band edges and energy band diagram alignment of the perovskite oxide structures with widely used photoactive layers,  $\text{SrTiO}_3$ ,  $\text{BaTiO}_3$ , and  $\text{CaTiO}_3$  emerge as promising materials to be applied as electron transporting layer (ETL) in the structure of the PSCs and Per-SCs. The findings also reveal that  $\text{SrTiO}_3$  and  $\text{CaTiO}_3$  exhibit the greatest electron mobility, making them more appropriate candidates for ETL. The minimal exciton binding energy found in  $\text{SrTiO}_3$  signifies its high separability and enhances its suitability for efficient carrier generation as the most effective ETL. The results obtained from optical parameters confirmed that the investigated compounds are appropriate candidates for TCE and CTL as they demonstrate low optical conductivity and absorptivity, minimal refractive index, and reflectivity in the solar range of the light spectrum (1–4 eV). The calculated elastic parameters verified that  $\text{SrTiO}_3$  and  $\text{CaTiO}_3$  are mechanically and thermally stable, which further supports their potential function in solar cells.



## 1. INTRODUCTION

Research into photovoltaic (PV) technology has progressed considerably in recent decades because of ever-increasing interest in renewable energy. The objective is to develop new nontoxic, and abundant materials that can be applied in the process of sunlight conversion into electricity.<sup>1</sup> Although crystalline silicon is one of the most heavily investigated PV materials currently leading the market, the high energy demand to process it has made PV devices based on crystalline silicon very costly. For large-scale power generation and small-scale, portable, and remote technological applications, inexpensive PV devices are highly appealing. As a result, significant research is being conducted to find low-cost alternative materials.<sup>2</sup>

Over the past few years, multiple companies have been established to pave the way for the development and commercialization of emerging types of semiconductor-based solar cells, e.g. perovskite solar cells (Per-SCs) and a particular type of organic solar cell (OSC) known as polymer solar cells (PSCs). The architecture of PSCs and Per-SCs consists of a light-absorbent active layer sandwiched between a bottom transparent conductive electrode (TCE) and a top metal electrode (ME).<sup>3</sup> The selection of charge transporting layers (CTLs), including electron transporting layers (ETL) and hole

transporting layers (HTL), is a crucial aspect of the PSC and Per-SC fabrication process.<sup>4</sup> Suitable CTLs can be employed to adjust the energy level alignment at the electrode/photoactive layer interfaces and optimize the collection of charge carriers (e.g., electrons and holes) by adjusting the work function (WF) of the electrodes.<sup>5</sup> They also facilitate charge extraction by forming an Ohmic contact between the electrode and the active layer. Moreover, charge carrier recombination at the interface between the photoactive layer and the transporting layer can be reduced by modifying the interface and utilizing appropriate CTLs.<sup>6</sup> Adding HTL/ETL can regulate the polarity of electrodes, enhance charge selectivity, and promote interfacial stability between the active layer and the electrodes.<sup>5,6</sup> Although the fundamental objective of the electrodes is to collect and transport holes and electrons,

**Received:** June 10, 2024

**Revised:** August 12, 2024

**Accepted:** August 26, 2024

several other characteristics are equally significant and should be explored. An efficient TCE should have a number of features, including high optical transmittance, excellent electrical conductivity, low sheet resistance, suitable WF, high mechanical and thermal stability, and low cost, to be chosen as an appropriate electrode for the device architecture.<sup>7</sup> Currently, fluorine-doped tin oxide (FTO) and indium tin oxide (ITO) are the most commonly used TCEs in the construction of solar cells.

The overall performance and stability of PSCs and Per-SCs can be strongly affected by the structures and characteristics of the CTLs/TCE materials.

Metal oxides, employed as CTL and TCE materials, represent optimal characteristics such as exceptional chemical and thermal stability, appropriate dielectric constant, superior charge mobility, superconductivity, and favorable optical transparency, meeting the requirements for efficient, stable, affordable, and solution-processed solar cells.<sup>4,6,8</sup> Furthermore, they can be manufactured from low-cost precursors in a variety of ways, the majority of which are compatible with low-temperature processing.<sup>9</sup> Metal oxides have been frequently reported as CTLs,<sup>10–13</sup> TCEs,<sup>14,15</sup> buffer layers,<sup>16,17</sup> and absorbent materials in the active layer<sup>18–20</sup> of the OSCs and Per-SCs. As already mentioned, favorable energy level alignment with the active layer, high optical transparency, and electrical conductivity are the most significant traits that metal oxides should possess to be classified as appropriate CTLs and TCEs.<sup>21,22</sup> However, their fixed features, such as bandgaps, energy levels, transmittance, and conductivity are the main drawbacks. Due to the varying energy levels of active layer materials, these fixed characteristics cause inflexibility in most PSCs and Per-SCs applications.<sup>5,23</sup> Ternary metal oxides with tunable band structures can be attractive candidates to overcome these limitations via alternating their composition.<sup>24</sup>

Perovskite-type oxides are a class of ternary metal oxides that have recently received much interest from researchers worldwide owing to their simple structure and potential for a wide range of applications.<sup>25</sup> The general formula of the perovskites is  $ABX_3$ , where A and B are two cations with different atomic sizes. A is the bigger cation, belonging to the alkali or alkaline earth metals, B is a smaller transition metal element, and X represents an anion.<sup>25</sup> In an ideal cubic array of  $ABX_3$ , the cuboctahedral cavities are occupied by the A-site cations, while the B-site cations are in the center of the octahedral sublattice and have the six closest X-anion neighbors.<sup>26</sup> Based on the type of X element, perovskites are divided into two categories, i.e. perovskite oxides ( $X = O$ ) and halide-based perovskites ( $X = Cl, Br, I$ ).<sup>27</sup> Extensive research has been conducted on perovskite oxides ( $ABO_3$ ) due to their appealing physical attributes, encompassing ferroelectric, dielectric, pyroelectric, and piezoelectric activities, along with notable chemical characteristics, highlighting their substantial potential for various technological applications.<sup>28</sup> Many of their exciting properties originate from the high sensitivity of these compounds to chemical tuning, which changes their physical properties significantly as a result of very tiny changes in their chemical composition or crystal structure. A wide variety of modified compounds can be achieved by substituting A and/or B-site cations of the  $ABO_3$  perovskites with different cations to develop a particular property, such as optical transparency, conductivity, or catalytic activity.<sup>29</sup> Perovskite oxides exhibit a variety of electrical characteristics, ranging from insulating to semiconducting to metallic, based on the

band gaps derived from their electronic structures.<sup>30,31</sup> As such, perovskite oxides are promising materials for exploitation in many emerging technological applications, including water splitting, fuel cells, environmental catalysis, chemical sensors, magnetic devices, field-effect transistors, electronic devices, and energy storage and conversion.<sup>32,33</sup>

Perovskite-type oxides have been applied in solar cells due to their low price, high structural and thermodynamic stability, and exceptional electronic, catalytic, optical, magnetic, ferroelectric, and magneto-resistance features.<sup>34–36</sup> Wide band gap perovskite oxides ( $>2$  eV) can be employed as CTLs and TCE in solar cells,<sup>37</sup> and a considerable number of investigations have reported applying  $ABO_3$ s as CTLs,<sup>38–44</sup> and TCE<sup>45–48</sup> in the Per-SCs and a type of OSCs known as dye-sensitized solar cells (DSSCs), although only a limited number of works have reported the utilization of  $ABO_3$ s in PSCs.<sup>49</sup>

The titanate perovskites ( $ATiO_3$ ), which exist in four isomorphs, i.e. rhombohedral, orthorhombic, tetragonal, and cubic structures, have been widely studied both computationally,<sup>50,51</sup> and experimentally.<sup>52,53</sup> Often, first principle calculations are employed to compute the properties and structures of these compounds, e.g. their electronic band structure and ferroelectricity,<sup>54,55</sup> but for a number of industrial applications, e.g. laser technologies (mirrors, lenses, and optical windows), contactless temperature measurement, optics, heat transfer, and energy, photovoltaic and aerospace applications, it is also crucial to gain a comprehensive understanding of the optical properties (absorption, emission, transmission, and reflection).

The effects of some particular wide band gap titanate-based  $ABO_3$ s as CTL and TCE in Per-SCs and DSSCs have already been investigated,<sup>26,27,56</sup> but to our knowledge, there is no report on employing these compounds in PSCs.  $ATiO_3$  must possess a unique electronic structure, optical transparency, and mechanical and thermal stability characteristics to be used as a specific component of PSCs and Per-SCs.

Along with developments in other technologies, flexible solar panels are anticipated to generate specialized products that require lightweight, mechanical flexibility, and the capacity to be molded into complex shapes, such as roof-panels for electric vehicles, folding umbrellas, and camping tents.<sup>57,58</sup> Thin-film polymer and perovskite solar cells are lightweight and mechanically flexible, making them suitable for flexible substrates, where they should tolerate repeated bending processes.<sup>59</sup> However, only a limited number of works have reported the mechanical and thermoelectric properties of the titanate-based perovskite oxides studied in this work.

Prior research on titanates with the perovskite structure has mainly concentrated on the calculation of some properties of a few specific systems, i.e.,  $CaTiO_3$ ,<sup>60,61</sup>  $SrTiO_3$ ,<sup>62–64</sup> and  $BaTiO_3$ ,<sup>65,66</sup> with different crystal structures but it is not easy to compare the results directly because each study has used different computational settings. In this study,  $ATiO_3$  ( $A = Be, Mg, Ca, Sr, Ba$ ) was chosen to be able to compare the results through the most stable alkaline earth based titanate perovskite oxides, where we have employed calculations based on the density functional theory (DFT) to determine their structural, electronic, optical, thermal, and elastic properties. The elastic properties were evaluated to assess the flexibility and thermal stability of these materials for use in PSCs and Per-SCs structures to enhance their performance and lifetime. The findings of these calculations were utilized to evaluate the possibility of employing any of these perovskite-type oxides as the CTLs/TCE in PSCs and Per-SCs. Furthermore, in order to

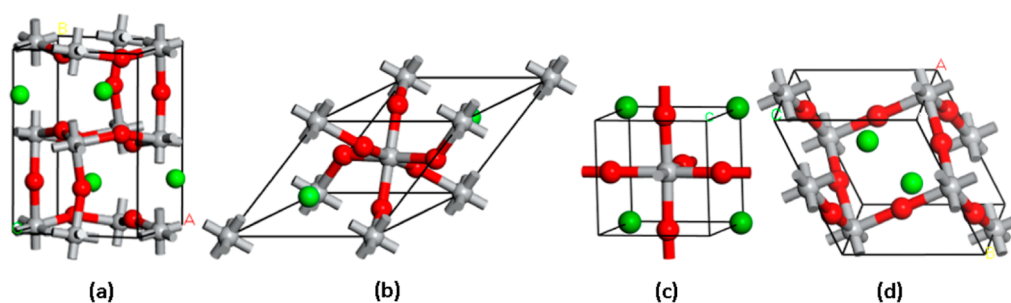


**Figure 1.** Crystal structures of the studied perovskite oxides with (a) orthorhombic ( $\text{CaTiO}_3$ ), (b) tetragonal ( $\text{BaTiO}_3$ ), (c) trigonal ( $\text{BeTiO}_3$ ,  $\text{MgTiO}_3$ ), and (d) monoclinic ( $\text{SrTiO}_3$ ) lattices. Alkaline earth, oxygen, and titanium atoms are shown in green, red, and gray spheres, respectively.

**Table 1.** Crystal Structure, Space Group, Volume, Lattice Parameters ( $a$ ,  $b$ ,  $c$ ,  $\alpha$ ,  $\beta$  and  $\gamma$ ), Formation Energy, and  $t$ -factor of Different Perovskite Bulk Crystal Structures<sup>a</sup>

formula	crystal structures (space group)	volume ( $\text{\AA}^3$ )	$a$ ( $\text{\AA}$ )	$B$ ( $\text{\AA}$ )	$C$ ( $\text{\AA}$ )	$A$ (deg)	$B$ (deg)	(deg)	$\Delta H_f$ (eV/atom) <sup>75,78</sup>	$t$ -factor
$\text{BeTiO}_3$	trigonal ( $R\bar{3}c$ )	91.878	5.405	5.405	5.405	52.45	52.45	52.45	-2.983	0.873
$\text{MgTiO}_3$	trigonal ( $R\bar{3}$ )	103.902	5.497	5.497	5.497	55.04	55.04	55.04	-3.188	0.845
			5.531 <sup>79</sup>	5.531 <sup>79</sup>	5.531 <sup>79</sup>					
$\text{CaTiO}_3$	orthorhombic $Pnma$	225.804	5.498	7.653	5.366	90.00	90.00	90.00	-3.367	0.983
			5.440 <sup>80</sup>	7.637 <sup>80</sup>	5.378 <sup>80</sup>					
$\text{SrTiO}_3$	monoclinic ( $C2/m$ )	120.929	5.537	5.537	5.557	119.87	119.87	90.00	-3.354	0.997
			5.579 <sup>79</sup>	5.579 <sup>79</sup>	5.579 <sup>79</sup>					
$\text{BaTiO}_3$	tetragonal ( $P4mm$ )	65.730	3.999	3.999	4.109	90.00	90.00	90.00	-3.288	0.999
				3.991 <sup>81</sup>	4.035 <sup>81</sup>					

<sup>a</sup>The available results from the literature are presented for comparison.

identify suitable materials for charge transport in collaboration with photoactive layers to facilitate the efficient separation of photogenerated charge carriers, we developed and investigated the consequences of energy band alignment between the photoactive layer and various ETLs and HTLs. Our results revealed that some of the studied  $\text{ATiO}_3$  compounds could be considered valuable materials for employment in the PSCs and Per-SCs structures, which would improve their mechanical and thermal stability and overall performance.

## 2. METHODOLOGY

In this work, we have employed the Vienna Ab initio Simulation Package (VASP),<sup>67</sup> for the DFT calculations. The Perdew–Burke–Ernzerhof (PBE) functional for the generalized gradient approximation was used for geometry optimization to determine the exchange and correlation energies within the projector augmented wave (PAW) method.<sup>68,69</sup> We have employed Grimme’s DFT-D3 method to include the long-range Van der Waals (vdW) forces to improve the energy description of the system.<sup>68,70</sup> The electronic properties including valence band maximum (VBM) and conduction band minimum (CBM) energy edges of the alkaline earth-based titanates and their optical properties were predicted utilizing the HSE06 screened hybrid functional incorporating a 25% Hartree–Fock exchange.<sup>71</sup> To identify the valence band maximum (VBM) in bulk materials, we explored the slab model method for aligning energy levels in a vacuum from periodic plane wave calculations.<sup>72</sup>

The electron wave functions are expanded using plane waves as basis sets with a cutoff energy of 600 eV. The convergence criteria for the Hellmann–Feynman forces and tolerance limit for energy during structure optimization are set to 0.01 eV/ $\text{\AA}$  and  $10^{-5}$  eV, respectively. We conducted a spin-polarized

calculation and observed that it had no impact on the outcomes.

The elastic coefficients were calculated by generating 7 distorted structures for each strain pattern, including three positives and three negatives under the maximum strain amplitude of 0.015, where the structures are optimized with convergence criteria of total energy within  $1 \times 10^{-8}$  eV/atom, the ionic Hellmann–Feynman forces within  $1 \times 10^{-2}$  eV/ $\text{\AA}$  and maximum ionic displacement within  $1 \times 10^{-4}$   $\text{\AA}$ .

The elastic and thermal properties were calculated using VASPKIT,<sup>73</sup> and the spatial dependence figures of the elastic properties were visualized by ELATE.<sup>74</sup>

## 3. RESULTS

**3.1. Structural Properties.** The crystal structures of the studied perovskites are shown in Figure 1. The structures are taken from the Open Quantum Materials Database (OQMD), as the most stable structures according to the calculated formation energies.<sup>75</sup> We have studied perovskite oxides with the general formula  $\text{ATiO}_3$ , where A includes elements of the second group of the periodic table, including the alkaline earth metals Be, Mg, Ca, Sr, and Ba. The structures have different crystal lattices, i.e., orthorhombic ( $\text{CaTiO}_3$ ), tetragonal ( $\text{BaTiO}_3$ ), trigonal ( $\text{BeTiO}_3$ ,  $\text{MgTiO}_3$ ), and monoclinic ( $\text{SrTiO}_3$ ) phases. The structural details and formation energies of the studied perovskite structures are presented in Table 1. Our recent findings revealed that some of these features are very close to what has been found in other studies.

The stability of the perovskite oxide structures is estimated by the most popular and successful geometric ratio known as the tolerance factor ( $t$ -factor) according to the Goldschmidt method in eq 1<sup>76</sup>

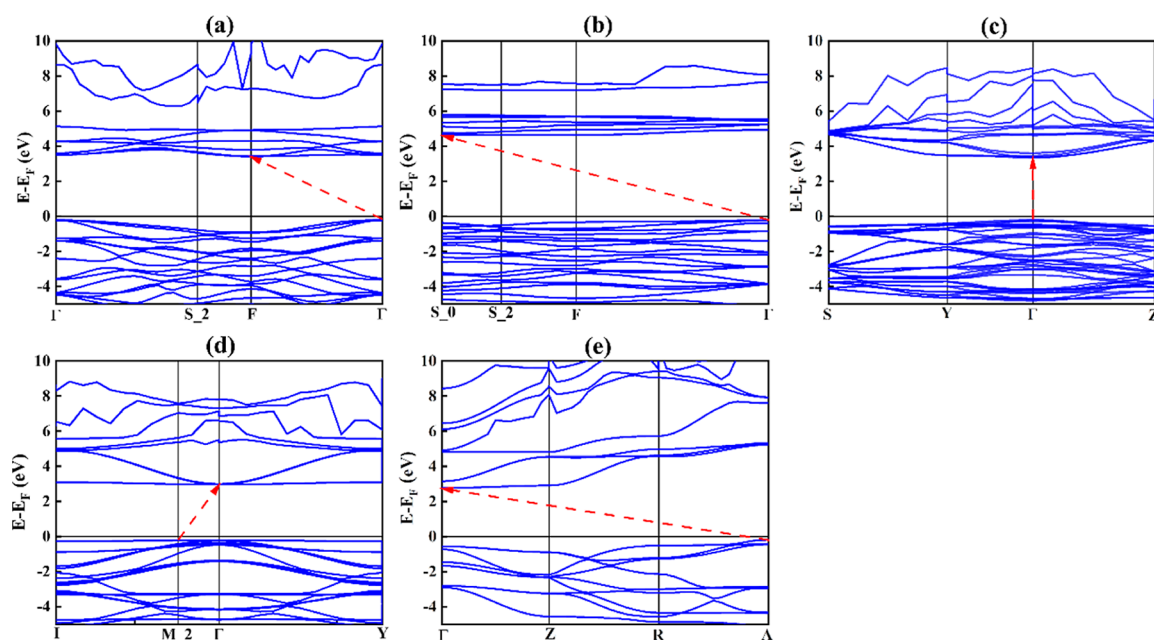


**Figure 2.** Band structure for (a) BeTiO<sub>3</sub>, (b) MgTiO<sub>3</sub>, (c) CaTiO<sub>3</sub>, (d) SrTiO<sub>3</sub> and (e) BaTiO<sub>3</sub>. The Fermi level is set to zero. The bandgaps of semiconductor structures are shown with red dashes.

$$t = \frac{\langle r_A \rangle + \langle r_O \rangle}{\sqrt{2}(\langle r_B \rangle + \langle r_O \rangle)} \quad (1)$$

where  $\langle r_A \rangle, \langle r_B \rangle$  and  $\langle r_O \rangle$  are the averages of the ionic radii of A, B, and O atoms.

The assessment of stability using the  $t$ -factor is often the initial step in designing novel perovskites for various applications. This factor predicts whether or not A cations are capable of entering the areas between generated octahedral structures to fill the structure corners.<sup>26</sup> If the  $t$ -factor changes from 0.8 to 1.1, the perovskite structure could be empirically formed with appropriate structural stability. While the BX<sub>6</sub> octahedra can be tilted, and the symmetry can be reduced in the lower portion of this range, they may still be distorted in the upper section. If the  $t$ -factor > 1.1, it means that the A site cation is too big, which usually inhibits the formation of a perovskite. If the  $t$ -factor < 0.8, the A site cation is too small, which can frequently lead to alternative structures.<sup>77</sup> As Table 1 shows, the  $t$ -factor is in the range of 0.84–0.99 for the studied compounds, confirming the stability of the structures.

**3.2. Electronic Properties.** For application as CTLs, perovskite oxides must have a wide bandgap so that more light can reach the photoactive layer.<sup>82</sup> The bandgap is the energy difference between the valence band maximum (VBM) and the conduction band minimum (CBM). The bandgap and energy levels of perovskite oxides directly influence the efficiency of PSCs and Per-SCs.<sup>24</sup> Perovskite oxides possessing a wide bandgap can be employed as the ETL and HTL in PSCs and Per-SCs.<sup>42,49</sup> DFT calculations were used to estimate the electronic structure and intrinsic features of the different perovskite oxides, including energy levels, bandgap, band structure, Fermi energy, and the density of states.

The HSE06 hybrid functional is used to evaluate the band structure (BS) and density of states (DOS) of ATiO<sub>3</sub> (A = Be, Mg, Ca, Sr, and Ba) perovskites. Figure 2a–e shows the band diagrams for all the considered ATiO<sub>3</sub> systems. In some of the calculated band structures, the valence band maxima appear flat. This phenomenon is not unique to this study and can be

attributed to specific electronic interactions and crystal structure configurations within the perovskite oxides. Similar flat bands have been reported in the literature for related materials, often due to strong electronic correlations and specific atomic arrangements.<sup>83–86</sup> Our findings align well with previous theoretical predictions, demonstrating consistency with established results while also providing novel insights into the electronic properties of these perovskite oxides.<sup>83,87–90</sup>

Moreover, the energy of the VBM and CBM plus the energy gap around the Fermi level are summarized in Table 2, where they are in agreement with the reported band gaps from other studies.

**Table 2.** Band Gaps ( $E_g$ ), and the Valence and Conduction Band Edges Energies ( $E_{\text{VBM}}$  and  $E_{\text{CBM}}$ ) in eV of Perovskite Oxides Structures

formula	band gap	$E_g$	$E_{\text{VBM}}$	$E_{\text{CBM}}$
BeTiO <sub>3</sub>	indirect	3.618	−7.63	−4.02
		3.31–3.61 <sup>87</sup>		
MgTiO <sub>3</sub>	indirect	4.852	−8.03	−3.18
		4.4 <sup>91</sup>		
CaTiO <sub>3</sub>	direct	3.535	−7.14	−3.60
		3.5 <sup>83</sup>		
SrTiO <sub>3</sub>	indirect	3.193	−6.86	−3.66
		3.2 <sup>89</sup>		
BaTiO <sub>3</sub>	indirect	2.960	−6.67	−3.71
		3.23 <sup>88</sup>		

More information can also be deduced from the direct or indirect characters of the bandgaps in Figure 2. In CaTiO<sub>3</sub>, electrons and holes recombine at the single symmetry point  $\Gamma$  of the Brillouin zone for the direct energy gap. In contrast, there are indirect band gaps of  $\Gamma \rightarrow \text{F}$ ,  $\Gamma \rightarrow \text{S}_{-0}$ ,  $\text{M}_{-2} \rightarrow \Gamma$ , and  $\text{A} \rightarrow \Gamma$  in BeTiO<sub>3</sub>, MgTiO<sub>3</sub>, SrTiO<sub>3</sub>, and BaTiO<sub>3</sub>, respectively. The obtained results are comparable with other works performed in this area.<sup>50,54,61,62,64,83,87–89,91,92</sup> All five compounds behave as semiconductors, and their bandgaps

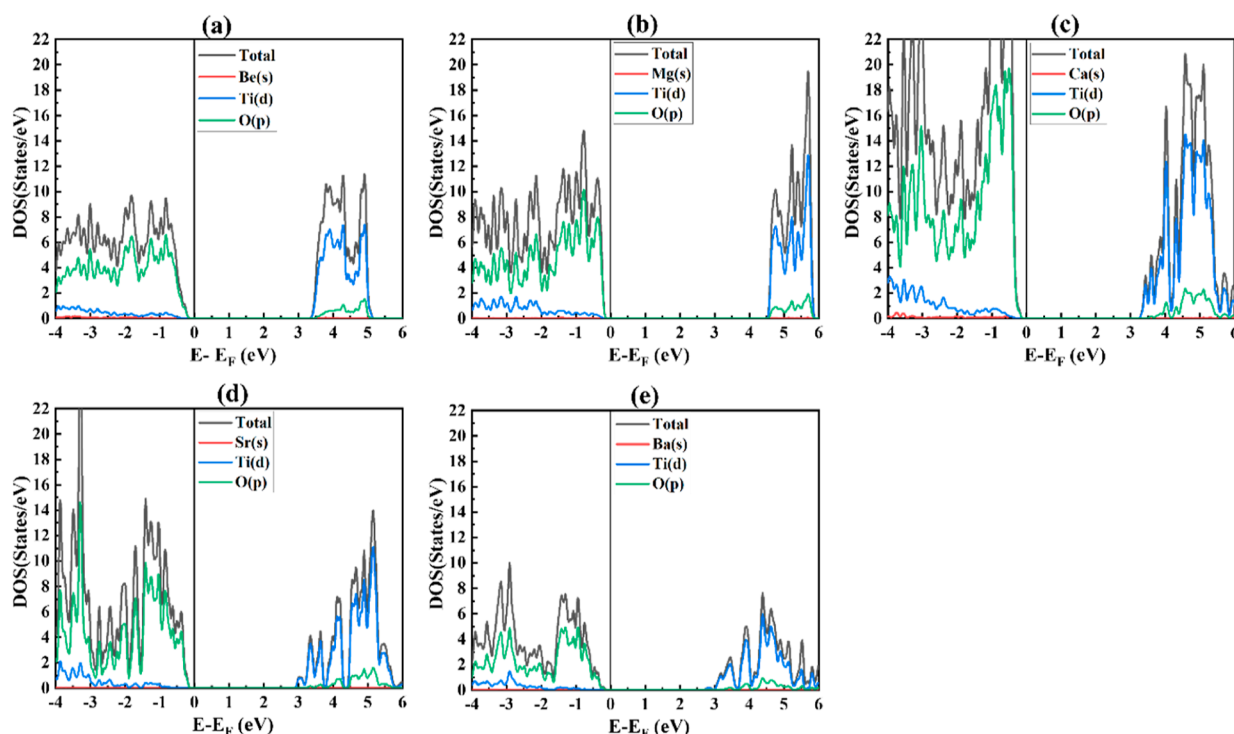


**Figure 3.** Total and Partial density of states for (a)  $\text{BeTiO}_3$ , (b)  $\text{MgTiO}_3$ , (c)  $\text{CaTiO}_3$ , (d)  $\text{SrTiO}_3$ , and (e)  $\text{BaTiO}_3$ . The Fermi level is set to zero.

increase from  $\text{BeTiO}_3$  to  $\text{MgTiO}_3$ , while decreasing from  $\text{MgTiO}_3$  to  $\text{BaTiO}_3$ . Thus, all studied perovskite oxides with a wide bandgap could be considered suitable candidates to be employed as CTL or TCE in PSCs and Per-SCs, since they can provide high optical transparency, so more incident light can reach the active layer.

The total and projected DOS plots for the alkaline earth metal titanate perovskite structures are shown in Figure 3 (a)–(e). The DOS results of the electronic properties are consistent with the BS results. As shown in Table 2, the calculated bandgaps of  $\text{BeTiO}_3$ ,  $\text{MgTiO}_3$ ,  $\text{CaTiO}_3$ ,  $\text{SrTiO}_3$ , and  $\text{BaTiO}_3$  are 3.618, 4.852, 3.535, 3.193, and 2.960 eV, respectively. The PDOS plots of  $\text{ATiO}_3$  ( $A = \text{Be, Mg, Ca, Sr, Ba}$ ) illustrate that the p orbitals of the O atoms occupy the VB, and the d orbitals of the Ti atoms have higher peaks in the CB.

**3.2.1. Band Alignment and Working Mechanism of PSC and Per-SC.** The structural design of PSCs and Per-SCs involves a light-absorbing photoactive layer positioned between TCE and ME. The classification of these devices into normal or inverted architectures is determined by the positioning of HTL and ETL and the direction of carriers' transportation.<sup>3</sup> Considering the identical characteristics and roles of CTLs in PSCs and Per-SCs, a large number of similar materials, such as nickel oxide and zinc oxide, have been employed as HTL and ETL in the structure of these photovoltaic devices, resulting in comparable outcomes.<sup>4,5</sup>

Figure 4 illustrates the structure of PSC and Per-SC, incorporating commonly utilized TCEs such as FTO and ITO, along with MEs (e.g., Ag, Au, and Al), frequently employed HTLs and photoactive layers during their fabrication process. The energy band alignment values are derived from both experimental and computational studies.<sup>93–99</sup> By assessing the energy level alignment of the used photoactive layers and VBM and CBM energy edges of alkaline earth-based titanates, these materials can be employed as effective ETL in the construction

of both PSCs and Per-SCs. Since the working mechanisms of normal and inverted PSCs, as well as Per-SCs, except for opposing carrier transport directions, are comparable, the normal structure of these devices is used to illustrate their operational mechanisms. The inverted structures can be found in Figure S1a,b. As depicted in Figure 4, all the investigated compounds, acting as semiconductors, can be utilized as ETLs in the fabrication of PSCs and Per-SCs. Notably, the CBM energy edges of  $\text{CaTiO}_3$ ,  $\text{SrTiO}_3$ , and  $\text{BaTiO}_3$  are more closely aligned with the LUMO energy level of the applied photoactive layers. This alignment is anticipated to result in improved charge extraction and transportation from the photoactive layer to the ETL composed of the examined perovskite oxides as supported by some of the reported experimental findings.<sup>42–44,48,100–103</sup>

When the photoactive layer is under light irradiation, excitons are generated and easily dissociate into free carriers (electrons and holes) due to the low exciton binding energy of common absorber materials. Following this, the built-in electric field and high carrier mobility within the photoactive layer facilitate the transport of electrons and holes to the interfaces with the ETL and HTL, respectively. Subsequently, a well-matched energy level alignment enables the injection of electrons and holes into the conduction band and valence band of ETL and HTL, respectively. Ultimately, electrons and holes are collected at the electrodes, where their WF needs to align well with the CBM and VBM of ETL and HTL, respectively, to ensure efficient collection. Throughout the operation of these devices, processes like charge transport, extraction, and collection are often accompanied by charge recombination, a phenomenon closely linked to efficiency and stability. This strongly emphasizes the pivotal role of different layers energy level alignment in achieving efficient and stable solar cells.

**3.2.2. Charge Mobility.** For prospective photoactive materials, it is crucial not only to possess a compatible energy

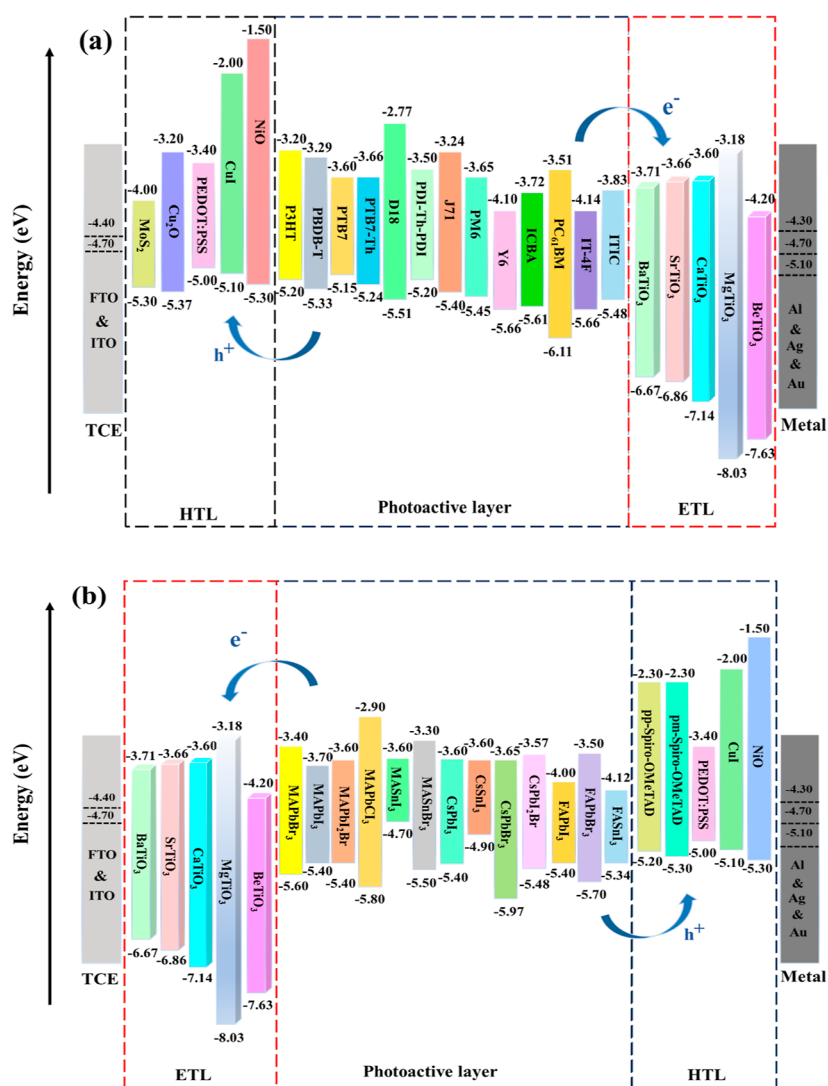


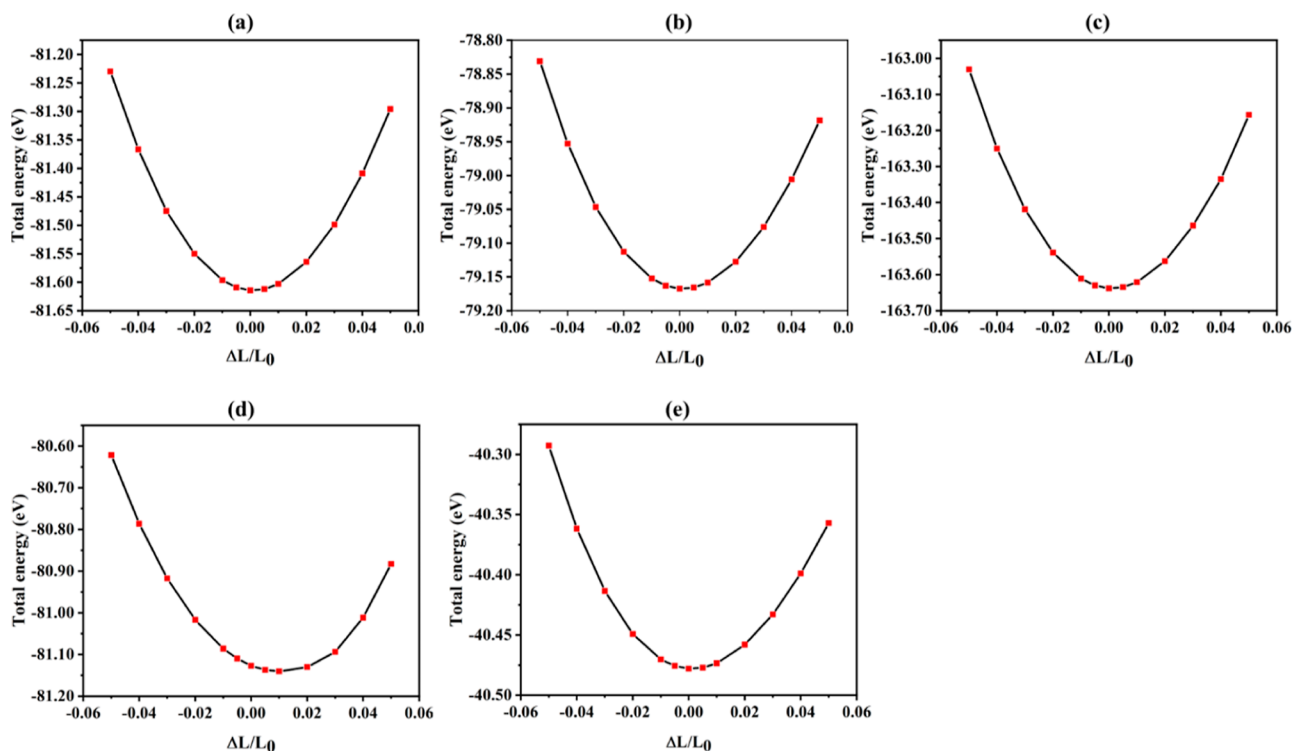
Figure 4. Energy level diagram of a normal (a) PSC and (b) Per-SC.

Table 3. Calculated Effective Mass ( $m^*/m_0$ ), Deformation Potential Constant ( $E_1$ ), 3D Elastic Constant ( $C^{3D}$ ), Carrier Mobility ( $\mu$ ), Relaxation Time ( $\tau$ ), and Exciton Binding Energy ( $E_b$ ) for Electrons and Holes along the Transport Direction

structure	type	$m^*/m_0$	$E_1$ (eV)	$C^{3D}$ (GPa)	$\mu$ ( $\text{cm}^2 \text{ s}^{-1} \text{ V}^{-1}$ )	$\tau$ (fs)	$E_b$ (meV)
BeTiO <sub>3</sub>	electron	2.193	-11.35	490.71	32.66	40.72	307.81
	hole	2.216	-7.72	490.71	68.82	86.71	
MgTiO <sub>3</sub>	electron	3.412	-8.30	375.02	15.45	29.97	1856.11
	hole	7.317	-7.25	375.02	3.01	12.53	
CaTiO <sub>3</sub>	electron	0.715	-9.23	308.20	309.27	125.72	235.39
	hole	0.254 <sup>118</sup>	-5.89	308.20	233.5 <sup>118</sup>	308.18	
SrTiO <sub>3</sub>	electron	2.586	-9.41	401.86	209.60	157.49	129.12
	hole	0.455	-6.76	401.86	608.81	305.79	
BaTiO <sub>3</sub>	electron	1.252	-9.04	298.16	429.58	31.23	258.28
	hole	2.544	-6.59	298.16	21.59	389.54	
	hole	2.82 <sup>120</sup>			950.24		

level but also to exhibit a reasonably high carrier mobility. Earlier studies confirmed that elevated electron mobility plays a pivotal role in swiftly extracting and transporting photo-generated electrons, enhancing the current density, overall efficiency, and exceptional photovoltaic properties.<sup>104–108</sup>

In the realm of inorganic semiconductors, the coherent wavelength of thermally activated electrons or holes approaches the acoustic photon wavelength at room temperature, significantly surpassing their lattice constant. In the low-energy regime, the scattering of thermal electrons or holes is chiefly influenced by the coupling between electrons and



**Figure 5.** Correlation between total energy and lattice dilation along the transport direction for (a) BeTiO<sub>3</sub>, (b) MgTiO<sub>3</sub>, (c) CaTiO<sub>3</sub>, (d) SrTiO<sub>3</sub>, and (e) BaTiO<sub>3</sub>.

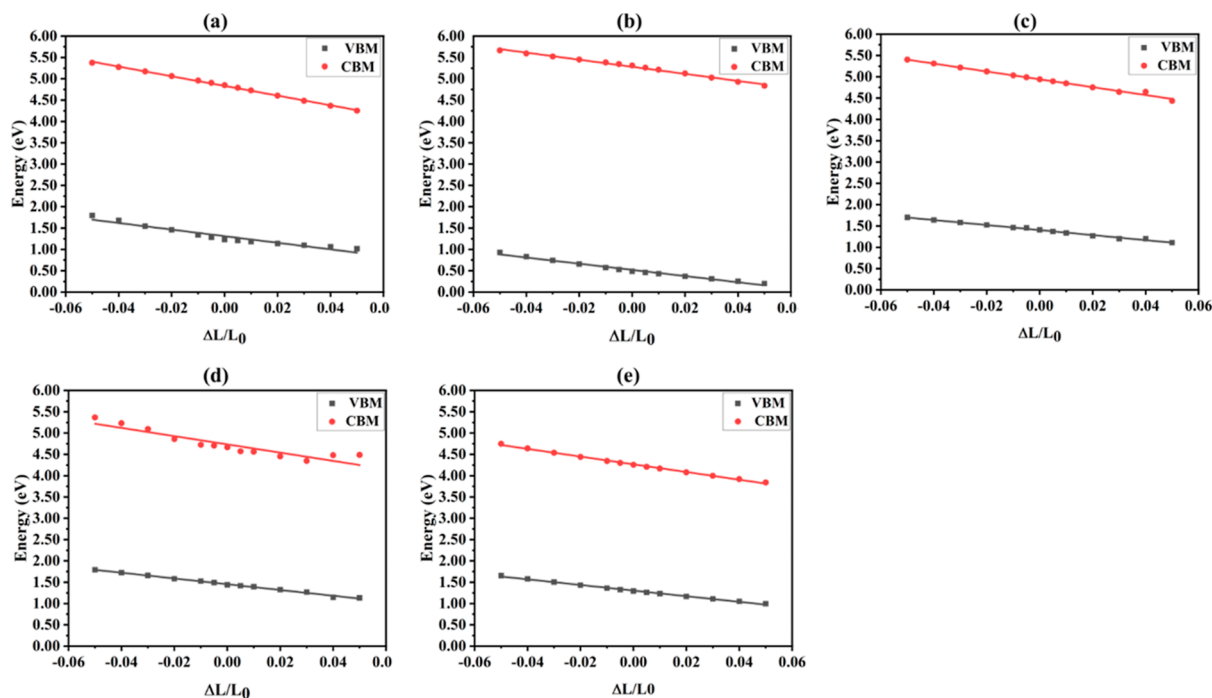


**Figure 6.** Shifts in band energies, including VBM and CBM, in response to uniaxial strain along the transport direction, for (a) BeTiO<sub>3</sub>, (b) MgTiO<sub>3</sub>, (c) CaTiO<sub>3</sub>, (d) SrTiO<sub>3</sub> and (e) BaTiO<sub>3</sub>.

acoustic phonons.<sup>109,110</sup> This interaction can be evaluated using the deformation potential (DP) theory formulated by Bardeen and Shockley.<sup>111</sup> Building upon the effective mass approximation, the mobility ( $\mu$ ) of carriers in three-dimensional materials can be mathematically represented as

$$\mu^{3D} = \frac{(8\pi)^{1/2} \hbar^4 e C^{3D}}{3(m^*)^{5/2} (k_B T)^{3/2} E_1^2} \quad (2)$$

where  $e$  is the electronic charge,  $\hbar$  is the reduced Planck constant,  $k_B$  is the Boltzmann constant, and  $T$  is the room temperature ( $T = 300$  K).  $m^*$  is the charge carrier effective mass in the transport direction, which can be calculated by the

finite difference method using the equation  $m^* = \hbar^2 / (\partial^2 E(k) / \partial k^2)$ , where  $E_k$  is the band-edge eigenvalues, and  $k$  is the wave vector magnitude. The 3D elastic constant, denoted as  $C^{3D}$ , is defined as the second derivative of the total energy ( $E$ ) with respect to the applied uniaxial strain ( $\delta$ ), divided by the equilibrium cell volume ( $V_0$ ). In mathematical terms, it can be expressed as  $C^{3D} = [(\partial^2 E / \partial \delta^2) / V_0]$ , where  $V_0$  represents the volume of the cell at equilibrium,  $E$  is the total energy, and  $\delta$  is the applied uniaxial strain.

The DP constant, denoted as  $E_1$ , is a proportionality constant linked to the shift in the band edge caused by an applied strain along the transport direction. Mathematically,  $E_1$  is defined as  $\Delta E_i / (\Delta L / L_0)$ , where  $\Delta E_i$  represents the energy change of the  $i$ th band resulting from lattice dilation  $\Delta L / L_0$  along the transport direction. This calculation is performed with a step size of  $\pm 1.0\%$ .

As indicated in eq 2, the effective mass plays a crucial role in determining carrier mobility. The computed values for the electron and hole effective masses ( $m^* / m_0$ ) along the transport direction for each structure are presented in Table 3, which agree with those of other available studies presented in the Table for comparison. All structures have larger hole effective masses than those of electrons, which means their electron transport abilities are better than their hole transport abilities except BaTiO<sub>3</sub>, with larger electron effective mass. The electron effective mass of MgTiO<sub>3</sub> is determined to be  $3.412m_0$ , making it the highest and leading to lower electron mobility. Conversely, SrTiO<sub>3</sub> exhibits the smallest electron effective mass, measuring  $0.455m_0$ , resulting in the highest electron mobility.

Carrier mobility is also significantly influenced by the 3D elastic constant ( $C^{3D}$ ) and DP constant ( $E_1$ ). To calculate  $C^{3D}$  and  $E_1$ , the lattice cell has been subjected to both a 5% dilation and compression along the transport direction. Total energies and positions of the VBM and CBM are determined concerning the extent of dilation and compression. At each step of dilation and compression, all atomic positions are fully relaxed. Electronic energies are obtained using the HSE06 hybrid functional. In Figure 5, the total energy variation is illustrated concerning applied uniaxial strain along the lattice direction. The determination of  $C_{3D}$  involves fitting the curve depicting energy versus strain. Figure 6 displays the shifts in both VBM and CBM as a function of uniaxial strain. The calculation of  $E_1$  involves determining the slope of the fitted lines in this representation. With the determined values for  $m^*$ ,  $C^{3D}$ , and  $E_1$ , the calculated electron mobilities for all structures are presented in Table 3, where they are compared with the results of the available studies. Based on the results, the electron mobilities for MgTiO<sub>3</sub> and SrTiO<sub>3</sub> are shown to be 15.45 and 608.81 cm<sup>2</sup> s<sup>-1</sup> V<sup>-1</sup>, which means that MgTiO<sub>3</sub> and SrTiO<sub>3</sub> have the lowest and highest electron transport abilities, respectively. The results also indicate that the lowest and highest hole mobilities and transport abilities belong to MgTiO<sub>3</sub> and BaTiO<sub>3</sub>, with hole mobility values of 3.01 and 950.24 cm<sup>2</sup> s<sup>-1</sup> V<sup>-1</sup>, respectively.

It is noteworthy to mention that the calculated carrier mobilities of these alkaline earth titanate oxide perovskites are comparable with those of many presently popular solar absorbers and semiconductor materials, including Si ( $1.5 \times 10^3$  cm<sup>2</sup> s<sup>-1</sup> V<sup>-1</sup>),<sup>112</sup> TiO<sub>2</sub> ( $5.24 \times 10^{-2}$  cm<sup>2</sup> s<sup>-1</sup> V<sup>-1</sup>),<sup>113</sup> CsPbI<sub>3</sub> ( $430$  cm<sup>2</sup> s<sup>-1</sup> V<sup>-1</sup>),<sup>114</sup> PbSe ( $1140$  cm<sup>2</sup> s<sup>-1</sup> V<sup>-1</sup>),<sup>115</sup> and PbTe ( $1508$  cm<sup>2</sup> s<sup>-1</sup> V<sup>-1</sup>).<sup>116</sup> In summary, when compared to

existing materials, these materials are anticipated as promising candidates to replace traditional semiconductors as the CTL.

The anisotropic relaxation time ( $\tau$ ) can be determined by utilizing the elastic constant ( $C^{3D}$ ), the DP constant ( $E_1$ ), and the effective mass ( $m^*$ ). The relationship is expressed as  $\tau = \mu m^* / e$ . The calculations for carrier mobility and relaxation time are conducted at room temperature, typically set at 300 K. The results are consistent with the calculated results of electron mobility, where the longest and shortest relaxation time belong to SrTiO<sub>3</sub> and MgTiO<sub>3</sub> with values of 157.49 and 29.97 fs, respectively.

To enhance the investigation of carrier mobility, we additionally compute the exciton binding energy. This energy is determined using the Wannier–Mott formula<sup>117</sup>

$$E_b = \frac{m_e m_h R_y}{m_0 (m_e + m_h) \epsilon_s^2} \quad (3)$$

In the given context, the variables are defined as follows:  $\epsilon_s$  represents the static dielectric constant (the value of the dielectric function at zero energy),  $m_e$  and  $m_h$  stand for the electron and hole effective masses in the transport direction, and  $R_y$  is the Rydberg energy constant with a value of 13.6057 eV. As per the information presented in Table 3, it is observed that the exciton binding energy in the SrTiO<sub>3</sub> is merely 129.12 meV, making it the most easily separable and conducive to carrier generation. In contrast, the exciton binding energy in MgTiO<sub>3</sub> is the highest, with the value of 1856.11 meV, posing challenges in separation and exerting a negative impact on carrier mobility. These findings align with the calculated results of carrier mobility, where SrTiO<sub>3</sub> and MgTiO<sub>3</sub> have the highest and lowest values, respectively.

**3.3. Optical Properties.** Optical properties are directly influenced by fundamental features such as the material's bandgap. Therefore, in addition to the investigation of the electronic structure, it is crucial to understand how electromagnetic radiation interacts with materials, i.e., absorption, transmission, reflection, and emission. Investigating the optical characteristics of solids is a valuable method to interpret their interaction with incident photon energy, which offers a predictive route to using new materials in photovoltaic devices.<sup>1,121</sup> In contrast to the extensive experimental efforts, few simulations on electrical and optical properties have been performed to optimize the ETL and HTL features to enhance device performance, even though the photovoltaic performance of PSCs and Per-SCs is highly dependent on the optical and electronic characteristics of CTLs.<sup>122,123</sup>

Since optical properties depend upon the dielectric constant, we discuss the dielectric constants  $\epsilon(\omega)$  with real,  $\epsilon_1(\omega)$ , and imaginary parts,  $\epsilon_2(\omega)$ , along with other important optical parameters, including the refractive index,  $n(\omega)$ , extinction coefficient,  $k(\omega)$ , reflectivity,  $R(\omega)$ , energy loss function,  $L(\omega)$ , adsorption coefficient,  $\alpha(\omega)$ , and optical conductivity,  $\sigma(\omega)$ , where  $\omega$  is the angular frequency of phonon.<sup>124</sup>

The sections below discuss these properties and where they are linked to each other, as explained by relevant equations. Some of the optical properties have already been studied for a few of the alkaline earth titanate perovskites, which will be helpful for the evaluation of our results.<sup>51,62,125,126</sup> The focus of our evaluation has been on the 1–4 eV range, recognized as the solar range, encompassing the visible region that constitutes the primary segment of sunlight. The inverse relation between photon energy (in eV), and wavelength (in

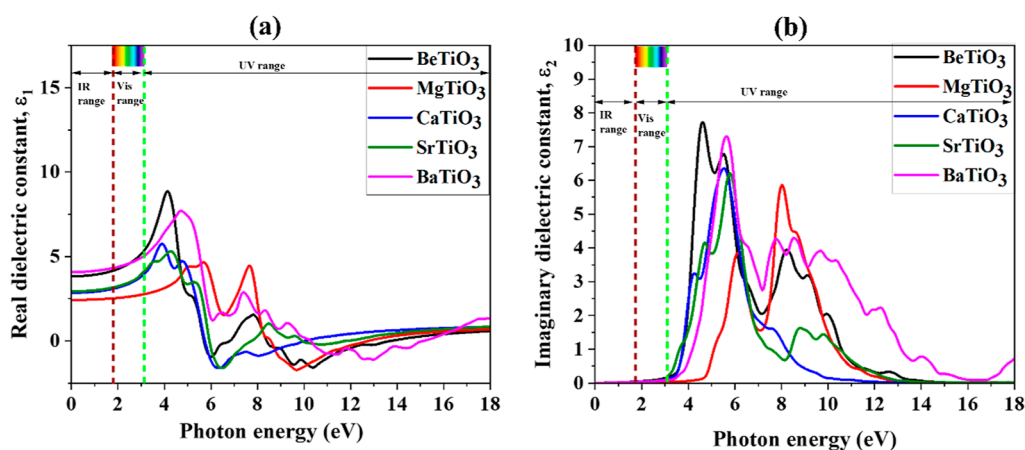


Figure 7. Real (a) and imaginary (b) dielectric constants for ATiO<sub>3</sub> (A: Be, Mg, Ca, Sr, and Ba).

nm) could be expressed as:  $E(\text{eV}) = \frac{1240}{\lambda(\text{nm})}$ .<sup>1</sup> Consequently, the visible region spans approximately from 1.77 to 3.10 eV.

**3.3.1. Dielectric Function.** The dielectric function is a key characteristic that is associated with the rate of charge-carrier regeneration in certain materials used in solar cells. The provided information offers a comprehensive understanding of the operational characteristics and efficiency of optoelectronic devices. Recombination rates in PSCs and Per-SCs could be reduced by increasing their dielectric constant.<sup>127</sup>

The frequency-dependent dielectric function comprises two well-known components, the real and imaginary parts, which are related to each other by  $\epsilon(\omega) = \epsilon_1(\omega) + i\epsilon_2(\omega)$ .

The absorptivity of the material can be predicted through the imaginary part,  $\epsilon_2(\omega)$ , by using the eq 4<sup>128</sup>

$$i\epsilon_2(\omega) = \left( \frac{e^2 \hbar^2}{\pi m^2 \omega^2} \right) \sum_{\nu,c} |\langle \psi_c | \hat{\epsilon}_j \cdot \vec{P} | \psi_\nu \rangle|^2 \delta(E_c - E_\nu - \hbar\omega) \quad (4)$$

where  $e$  and  $m$  are the charge and mass of an electron, respectively,  $\vec{P}$  indicates the momentum operator, and  $\hat{\epsilon}_j$  denotes the unit vector designating the direction of the external electromagnetic field of energy.  $E_\nu$  and  $\psi_\nu$  are the related valence energy and vacant wave function, respectively, whereas  $E_c$  and  $\psi_c$  are the conduction energy and filled wave functions, respectively.

The real component,  $\epsilon_1(\omega)$ , characterizes the dispersion and polarization characteristics of electromagnetic radiation and is calculated using  $\epsilon_2(\omega)$  via the well-known Kramers–Krönig relation as shown in eq 5:<sup>129</sup>

$$\epsilon_1(\omega) = 1 + \left( \frac{2}{\pi} \right) P \int_0^\infty \frac{\omega' \epsilon_2(\omega')}{\omega'^2 - \omega^2} d\omega' \quad (5)$$

where  $P$  is the principal value of the integral.

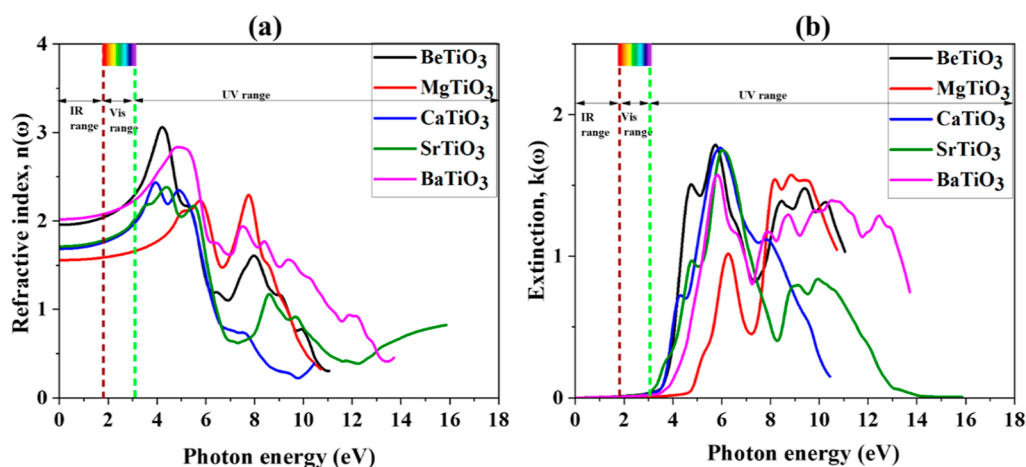
The real dielectric constants for all studied structures are illustrated in Figure 7 (a). The static values of the dielectric constants at zero energy,  $\epsilon_1(0)$  are listed in Table 4. At low photon energies, the real part of the dielectric function displays a greater value, and as the photon energy increases, this value falls quite sharply. Following a further increase in photon energy from the visible region to UV, negative values of  $\epsilon_1(\omega)$  appear, suggesting that perovskite structures demonstrate a notable reflection of incident light and poor transmission through their surface in the UV region, as reported in other studies.<sup>92,130</sup> The studied semiconductors consisting of alkaline

Table 4. Values of Dielectric Constant,  $\epsilon_1(0)$ , Refractive Index,  $n(0)$ , and Reflectance,  $R(0)$ , at Zero Energy and Maximum Values of Absorption Coefficient,  $\alpha_{\max}(\omega)$ , Optical Conductivity,  $\sigma_{\max}(\omega)$ , and Energy Loss Function,  $L_{\max}(\omega)$

name	$\epsilon_1(0)$	$n(0)$	$R(0)$	$\alpha_{\max}(\omega)$ (10 <sup>7</sup> /cm)	$\sigma_{\max}(\omega)$ (10 <sup>16</sup> /s)	$L_{\max}(\omega)$
BeTiO <sub>3</sub>	3.82	1.95	0.10	143.98	4.48	0.45
MgTiO <sub>3</sub>	2.42	1.55	0.04	148.48	6.15	0.47
CaTiO <sub>3</sub>	2.84	1.68	0.06	107.45	4.21	6.54
SrTiO <sub>3</sub>	2.92	1.71	0.06	108.54	4.39	3.96
BaTiO <sub>3</sub>	4.07	2.01	0.11	162.33	5.39	1.09

earth based titanates show a favorably positive value of the real dielectric constant in the solar range, consequently reflecting less from their surface. MgTiO<sub>3</sub> demonstrates the lowest  $\epsilon_1(0)$  and for all the investigated compounds, including MgTiO<sub>3</sub>, this value remains nearly constant across the solar range. Therefore, among the suggested compounds in the electronic structure section (Section 3.2), SrTiO<sub>3</sub> and CaTiO<sub>3</sub> exhibit the greatest transparency in the solar range, making them more suitable choices for CTL and TCE.

The behavior of the imaginary component of the dielectric function,  $\epsilon_2(\omega)$  in energy values of 0–18 eV is depicted in Figure 7b. The presence of various peaks in the spectrum could be attributed to the formation of electron–hole pairs for conduction, interband optical transitions occurring between the valence and conduction bands, and the collection of excitons from the free carriers. The last peak seen in higher energy regions is often referred to as the plasma frequency, with the corresponding peak being denoted as the plasmon peak. The variation in band gaps among these materials could be attributed to their inconsistent light responses.<sup>127</sup> In all structures, the positive values of  $\epsilon_2(0)$  and observed peaks in the UV region indicate interband transitions of electrons from their filled VB to the empty CB and the absorptive behavior of the compound. The intraband transitions have been ignored for these materials, as they were in former studies.<sup>131,132</sup> All studied compounds demonstrate light absorption in the middle section of the UV area. However, the imaginary part of the dielectric function exhibits a diminishing trend toward zero within a larger range of photon energy of the UV spectrum, indicating less interaction between materials and incident light in this region. In the instance of MgTiO<sub>3</sub>, the value of  $\epsilon_2(\omega)$  exhibits an increase slightly beyond the photon energy of 4 eV,



**Figure 8.** Refractive index (a) extinction coefficient (b) for ATiO<sub>3</sub> (A: Be, Mg, Ca, Sr, and Ba).

and the absorption of other examined semiconductors also proves to be zero in most parts of the solar range and rises slightly before 4 eV, effectively covering the solar range. This unique behavior renders previously proposed compounds of SrTiO<sub>3</sub> and CaTiO<sub>3</sub> as almost transparent materials within this range, positioning them favorably for use as CTL and TCE components in PSCs and Per-SCs. Light absorption is considered a limiting factor to applying these perovskite oxides as CTLs or TCEs.

**3.3.2. Refractive Index and Extinction Coefficient.** The refractive index is a crucial parameter in solar applications, significantly influencing how incident light interacts with materials and is essential for assessing the transparency of materials and their behavior when exposed to light.<sup>92,131</sup> The refractive index,  $n(\omega)$ , is calculated using the eq 6

$$n(\omega) = \left[ \frac{\varepsilon_1(\omega)}{2} + \sqrt{\frac{\varepsilon_1^2(\omega) + \varepsilon_2^2(\omega)}{2}} \right]^{1/2} \quad (6)$$

The spectra of the calculated refractive indices as they vary with photon energy are displayed in Figure 8a. The static refractive indices of the structures at zero energy,  $n(0)$ , are given in Table 4. Due to the relations between the real dielectric constant and the refractive index, variations in their values were expected to follow the same trends.<sup>130</sup> The gradual increase in the refractive index of the studied compounds is indeed a trend that has already been observed for the dielectric constants. Based on its electronic structure among all studied perovskite oxides, MgTiO<sub>3</sub>, SrTiO<sub>3</sub>, and CaTiO<sub>3</sub> show the lowest refractive index in the solar range, while MgTiO<sub>3</sub> demonstrates the highest value in the UV region at energy edge of 7.8 eV, which is consistent with  $\varepsilon_1(\omega)$ . In contrast, BeTiO<sub>3</sub> exhibits the greatest value at the energy edge of 4.2 eV. As photon energy rises to higher values (>8 eV),  $n(\omega)$  exhibits a steep decline across all examined structures, indicating reduced interactions between incoming light and the materials. The largest value of  $n(\omega)$  indicates that there could be significant interaction between incoming light photons and valence electrons during transmission, leading to significant polarization in the materials. Therefore, the smaller the value of  $n(\omega)$  the higher the transparency, which is in accordance with the role of a material as CTL or TCE. Therefore, it can be concluded that the proposed function of SrTiO<sub>3</sub>, and CaTiO<sub>3</sub> with a semiconductor nature as ETL in PSC and Per-SCs is

confirmed by the highest transparency observed in the solar range based on the refractive index calculations.

Furthermore, the ability of the surfaces of the studied materials to absorb incident photons at specific wavelengths of light is controlled by the extinction coefficient,  $k(\omega)$  which can be calculated by the eq 7<sup>131,133</sup>

$$k(\omega) = \left[ \frac{-\varepsilon_1(\omega)}{2} + \sqrt{\frac{\varepsilon_1^2(\omega) + \varepsilon_2^2(\omega)}{2}} \right]^{1/2} \quad (7)$$

The extinction coefficient,  $k(\omega)$ , versus the photon energy, is shown in Figure 8b, and it reflects the transition of the electrons from the VB to the CB in dielectric materials.<sup>125</sup> As can be seen, for all of the investigated compounds,  $k(\omega)$  remains almost zero in the most area of the solar range followed by several peaks throughout the UV region, indicating that the photons of incident light in the solar range are not alleviated, while the incident light has maximum diffusion into the compound in the UV region. As shown in Figure 8 (b), throughout the solar range, the lowest value of  $k(\omega)$  remained almost constant for the preferred compounds of SrTiO<sub>3</sub>, and CaTiO<sub>3</sub>, indicating the lowest absorption of incident radiation. The calculated  $k(\omega)$  emphasizes that the indicated compounds are promising ETL or TCE candidates for the PSCs and Per-SCs. These findings are in good agreement with previously reported results.<sup>62,92</sup> The calculated refractive index  $n(\omega)$  and extinction coefficient  $k(\omega)$  of the pure material are in agreement with experimental results.<sup>134</sup>

**3.3.3. Absorption Coefficient.** The absorption coefficient  $\alpha(\omega)$  is widely acknowledged as the most important optical characteristic in determining solar cell performance.<sup>127</sup> The power conversion efficiency of the resultant solar cell is strongly influenced by the absorption coefficient of the materials used in its fabrication. The rapid and efficient capture of incoming light is crucial in the active layer of PSCs and Per-SCs, necessitating a high absorption coefficient. On the other hand, in the case of CTLs and TCEs, it is desirable to have a low absorption coefficient, as this enables a larger portion of light to transmit through the layer and ultimately reach the active layer.<sup>127,135</sup> The absorption coefficient,  $\alpha(\omega)$ , describes the efficiency of the materials in absorbing photons of light with an energy of  $\hbar\omega$ , as given in eq 8.<sup>136</sup>

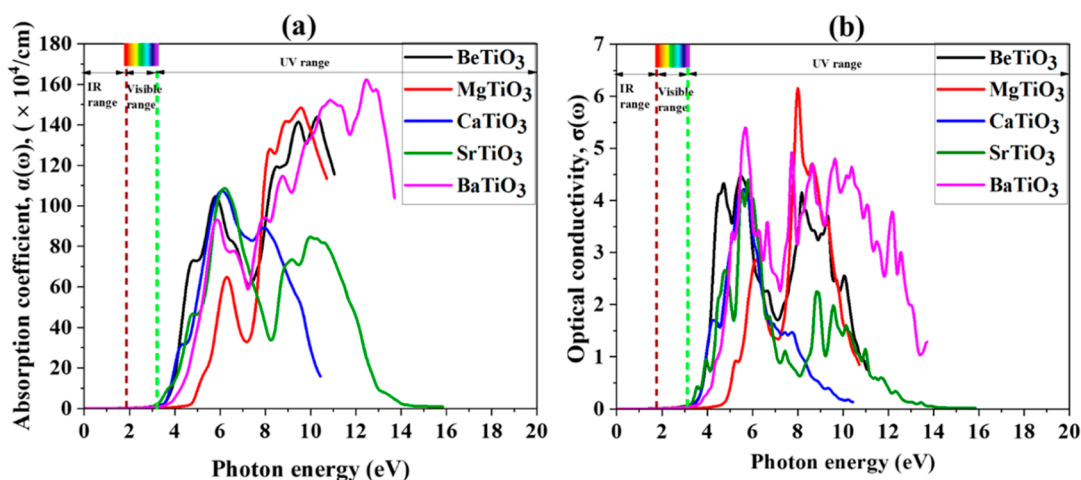


Figure 9. Absorption coefficient (a) optical conductivity (b) for ATiO<sub>3</sub> (A: Be, Mg, Ca, Sr, and Ba).

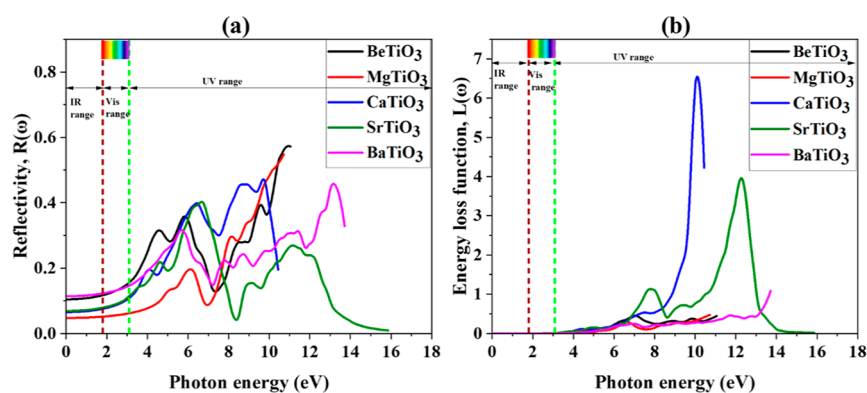


Figure 10. Reflectivity and (a) and energy loss function (b) for ATiO<sub>3</sub> (A: Be, Mg, Ca, Sr, and Ba).

$$\alpha(\omega) = 2\omega k(\omega) = 2\omega \left[ \frac{-\varepsilon_1(\omega)}{2} + \sqrt{\frac{\varepsilon_1^2(\omega) + \varepsilon_2^2(\omega)}{2}} \right]^{1/2} \quad (8)$$

Figure 9a shows the absorption spectra of all considered materials. It has been demonstrated that for all studied compounds, there is zero or negligible absorption in the solar range. This observation indicates that these materials, specifically the suggested compounds of SrTiO<sub>3</sub>, and CaTiO<sub>3</sub> are transparent, allowing most of the light in this region to pass through. Consequently, they are excellent candidates for use in ETL and TCE.<sup>130,137</sup> As can be seen,  $\sigma(\omega)$  increases gradually with increasing energy of the light in the UV region. Among the materials studied, BaTiO<sub>3</sub>, revealed the maximum absorption within the UV region at the energy edge of 12.5 eV. Therefore, it is the most absorptive material among all the studied perovskite oxides in the UV region of the electromagnetic spectrum, and as such, could be used as UV absorbers in photovoltaic and optoelectronic devices (see Table 4).

**3.3.4. Optical Conductivity.** When incident light interacts with the material surface, it leads to the generation of photoelectrons as a result of bond breaking. The conduction of these photoelectrons within the material is regulated by the optical conductivity, denoted as  $\sigma(\omega)$ .<sup>135</sup> The optical conductivity parameter,  $\sigma(\omega)$ , as a function of photon energy is illustrated in Figure 9b, characterizing the conductivity of the

material due to optical excitation caused by photons.<sup>138</sup> It is determined from the following eq 9<sup>139</sup>

$$\sigma(\omega) = \frac{\alpha(\omega)n(\omega)c}{4\pi} \quad (9)$$

The value of  $\sigma(\omega)$  is zero or negligible in the most range of solar range for all of the studied alkaline earth titanates, indicating no optical interaction and excitation for these materials, in this region of the electromagnetic spectrum. The results obtained for  $\sigma(\omega)$  agree with the optical parameters discussed above, confirming the potential application of investigated compounds as ETL and TCE in the PSCs and Per-SCs. The  $\sigma(\omega)$  values are consistent with the extinction coefficient and rise to higher values in the UV region. The maximum optical conductivities for all materials are listed in Table 4. MgTiO<sub>3</sub> can be considered the most conductive compound in this region of the electromagnetic spectrum, possessing the highest optical conductivity of  $6.15 \times 10^{16}$ .

**3.3.5. Reflectivity.** Reflectivity  $R(\omega)$ , plays a vital role as an optical property in determining the surface characteristics of materials employed in solar cell technology.<sup>127</sup> The reflectance behavior of photons at the material is explained by the  $R(\omega)$ , describing the portion of light reflecting from the material, as shown in Figure 10a and calculated from eq 10

$$R(\omega) = \frac{(n(\omega) - 1)^2 + k(\omega)^2}{(n(\omega) + 1)^2 + k(\omega)^2} = \left| \frac{\sqrt{\varepsilon} - 1}{\sqrt{\varepsilon} + 1} \right|^2 \quad (10)$$

The static values of reflectivity at zero energy,  $R(0)$ , for all mentioned materials, are listed in Table 4. Based on the obtained data, the reflectivity is very low for all the studied perovskite compounds in the solar range, while  $\text{MgTiO}_3$ ,  $\text{SrTiO}_3$ , and  $\text{CaTiO}_3$  demonstrate the lowest amounts of  $R(\omega)$  in this area. The data in this segment validates our prior results for other optical properties. As  $\text{SrTiO}_3$  and  $\text{CaTiO}_3$  display the lowest  $R(\omega)$ , and consequently, the highest transmission among all five semiconductors, it reinforces their proposed role in PSCs and Per-SCs.

The reflectivity of all studied perovskite oxides increases in the UV region, with  $\text{BeTiO}_3$  perovskites exhibiting the highest reflectivity at the energy edge of 11 eV. Therefore, in the UV region, all studied compounds reflect a considerable portion of the incident light.

**3.3.6. Energy Loss Function.** Ultimately, the dissipation of optical energy, whether through scattering, heating, or dispersion, is governed by the energy loss function  $L(\omega)$ , as illustrated in Figure 10b. The energy loss function is a representation of the energy lost by swiftly moving electrons because of the impact of electromagnetic light on materials. Plasma oscillations induce the separation of fast-moving electrons at lattice positions. When the maximum value of the energy loss function is reached, the electrons in this energy range are free to perform plasma oscillation rather than being confined to their lattice locations in response to incident light.<sup>132,135,140</sup> The energy loss function,  $L(\omega)$ , is calculated using eq 11

$$L(\omega) = \frac{\epsilon_2(\omega)}{\epsilon_1^2(\omega) + \epsilon_2^2(\omega)} \quad (11)$$

The peaks in the  $L(\omega)$  spectra represent the plasma resonance, where their associated frequencies are the corresponding plasma frequencies. Figure 10b shows that there are several loss peaks in the UV region of the electron energy loss (EEL) spectrum, while no peak is observed in the visible region for all studied compounds. The increments in photon energy lead to an increase in  $L(\omega)$ , indicating higher energy losses in the UV region. The maximum peaks for all structures are listed in Table 4. As can be observed, the most intensive plasmon peak of 6.54 at 10.12 eV is observed for  $\text{CaTiO}_3$  in the UV region.

The EEL spectrum has two distinct sections: the low-loss region (up to around 50 eV in energy loss) and the high-loss zone. Analysis in the valence region (<50 eV) provides information similar to that offered by optical spectroscopy.<sup>141</sup> Band structure and dielectric characteristics of the sample may be deduced from the low-loss spectrum, which includes the zero-loss peak and the plasmon peaks.<sup>141,142</sup> Following the previously described optical characteristics, the EEL spectrum shows no prominent plasmon peaks in the solar range for any of the studied semiconductors, making it clear that no interaction occurs between these compounds and the incident light in this region. As shown in Figure 10b, the EEL spectra for the proposed compounds of  $\text{SrTiO}_3$  and  $\text{CaTiO}_3$  stay zero in the whole range of the solar range and rise slightly thereafter. These calculations confirm our previous suggestions that these materials could be appropriate candidates to be used as CTL or TCE in solar cells.

Thus, the overall optical characteristics of the investigated materials, including minimum absorption, reflectivity, optical

conductivity, and least energy loss, make them promising compounds for applications in photovoltaic devices.

**3.4. Elastic and Thermal Properties.** While Per-SCs and PSCs have not yet provided their theoretical maximum efficiency, most research efforts in recent years have shifted from boosting efficiency to addressing the critical issue of device stability.<sup>143</sup> The stability of solar cells is affected by two major factors: (i) the thermal and humidity stability of the active layer, and (ii) the structural and mechanical stability of the solar cell constituents, primarily including the TCE and CTLs of the device structure which should be stable under external factors such as high pressure and elevated temperatures.<sup>10,143</sup> How a material responds when exposed to external factors such as pressure and strain is governed by the elastic properties of the material. Elastic constants are the dimensional constants that determine the relationship between stress and strain in a material. When a material is subjected to stress, its deformation can be estimated via the elastic constants.<sup>144</sup> Since stability is a major concern for the commercialization of PSCs and Per-SCs, the elastic constants and the derived elastic moduli were calculated for each of the perovskite oxides to evaluate their mechanical stability. Elastic constants are fundamental for understanding a material's mechanical properties and their impact on mechanical stability, hardness, plastic deformation, as well as properties like rigidity, strength, resilience, and ductility.<sup>135</sup> Less rigid materials with a lower modulus of elasticity are rubber-like; they distort quickly but rapidly return to their original shape. In contrast, stiffer materials with a higher modulus are dense and can absorb heavy loads.<sup>145</sup> As already mentioned, PSCs and Per-SCs must incorporate flexible materials into their structure to enable them to be used in new applications, such as roof panels for electric vehicles and folding umbrellas.

Each crystal structure with a certain symmetry has different numbers of independent elastic constants. The inverse of each stiffness tensor,  $c_{ij}$ , is the compliance tensor,  $s_{ij} = c_{ij}^{-1}$ . The crystal bulk modulus ( $B$ ), shear modulus ( $G$ ) Young's modulus ( $E$ ) and Poisson's ratio ( $\nu$ ) were calculated according to the Voigt, Reuss, and Hill approximations.<sup>146–148</sup> According to the Hill approximation, the bulk modulus ( $B_H$ ) and shear modulus ( $G_H$ ) are calculated according to eqs 12 and 13 as

$$B_H = \frac{1}{2}(B_V + B_R) \quad (12)$$

$$G_H = \frac{1}{2}(G_V + G_R) \quad (13)$$

where the two parameters of the bulk modulus and shear modulus, according to the Voigt and Reuss approximations<sup>147,148</sup>  $B_V$ ,  $B_R$ ,  $G_V$  and  $G_R$ , are averaged by employing eqs 14 to 17 as

$$B_V = \frac{1}{9}(C_{11} + C_{22} + C_{33}) + \frac{2}{9}(C_{12} + C_{13} + C_{23}) \quad (14)$$

$$B_R = \frac{1}{(S_{11} + S_{22} + S_{33}) + 2(S_{12} + S_{13} + S_{23})} \quad (15)$$

$$G_V = \frac{1}{15}(C_{11} + C_{22} + C_{33} - C_{12} - C_{13} - C_{23}) + \frac{1}{5}(C_{44} + C_{55} + C_{66}) \quad (16)$$

**Table 5.** Calculated Elastic Constants ( $C_{ij}$ , in GPa), Bulk Modulus (in GPa), Young's Modulus (in GPa), Shear Modulus (in GPa), Poisson's Ratio, Minimum Lattice Thermal Conductivity (in  $\text{W m}^{-1} \text{K}^{-1}$ ), and Debye Temperature (in K) Obtained from Hill Approximation of  $\text{ATiO}_3$  ( $A = \text{Be, Mg, Ca, Sr, and Ba}$ )

elastic parameters	BeTiO <sub>3</sub>	MgTiO <sub>3</sub>	CaTiO <sub>3</sub>	SrTiO <sub>3</sub>	BaTiO <sub>3</sub>
$C_{11}$	441.23	330.60	320.76	326.74	299.13
$C_{12}$	186.39	145.29	109.01	84.91	111.98
$C_{13}$	141.97	96.48	135.48	121.00	87.00
$C_{14}$	5.54	13.04			
$C_{15}$	0	5.12		-30.40	
$C_{22}$			343.53	326.79	
$C_{23}$			109.41	120.73	
$C_{25}$				3.96	
$C_{33}$	307.03	269.82	305.11	346.14	123.22
$C_{35}$				-28.66	
$C_{44}$	116.84	81.59	103.65	90.86	65.35
$C_{46}$				1.75	
$C_{55}$			110.16	84.27	
$C_{66}$	127.42	92.65	117.12	108.59	121.02
bulk modulus ( $B_H$ )	231.42	176.49	186.32	181.24	129.23
	245.40 <sup>54</sup>	193.49 <sup>54</sup>	189.61 <sup>54</sup>	184.26 <sup>54</sup>	178.52 <sup>54</sup>
Young's modulus ( $E_H$ )	305.47	228.87	268.67	252.74	185.47
	302.85 <sup>54</sup>	233.37 <sup>54</sup>	280.86 <sup>54</sup>	288.22 <sup>54</sup>	284.79 <sup>54</sup>
shear modulus ( $G_H$ )	119.32	89.13	106.65	99.70	73.55
	116.99 <sup>54</sup>	89.83 <sup>54</sup>	112.07 <sup>54</sup>	116.28 <sup>54</sup>	115.38 <sup>54</sup>
Poisson's ratio ( $\nu_H$ )	0.28	0.28	0.26	0.27	0.26
	0.29	0.30	0.25 <sup>54</sup>	0.24	0.23
Pugh's ratio	1.94	1.98	1.75	1.82	1.76
Cauchy's pressure	69.55	63.70	5.36	-5.95	46.63
anisotropy factor	0.91	0.88	0.98	0.75	0.69
Debye temperature ( $\theta_D$ )	888.60	732.70	761.70	641.80	603.00
minimum thermal conductivity ( $\kappa_{\min}$ )	0.20	0.19	0.36	0.28	0.18

$$G_R = [4(S_{11} + S_{22} + S_{33}) - 4(S_{12} + S_{13} + S_{23}) + 3(S_{44} + S_{55} + S_{66})]^{-1} \quad (17)$$

The Young's modulus ( $E_H$ ) and Poisson's ratio ( $\nu_H$ ) are calculated using the bulk modulus ( $B_H$ ) and shear modulus ( $G_H$ ) from the Hill scheme, using the following eqs 18 and (19)

$$E_H = \frac{9B_H G_H}{3B_H + G_H} \quad (18)$$

$$\nu_H = \frac{3B_H - 2G_H}{2(3B_H + G_H)} \quad (19)$$

Using the calculated Young's modulus ( $E_H$ ) and Poisson's ratio ( $\nu_H$ ) and crystal structure parameters, the theoretical minimum thermal conductivity ( $\kappa_{\min}$ ) was obtained as the lowest limit of the thermal conductivity value.<sup>149–151</sup> According to the Clarke model,<sup>152</sup> the theoretical minimum thermal conductivity can be calculated via eq 20

$$\kappa_{\min} = 0.87k_B \left( \frac{M}{n\rho N_A} \right)^{-2/3} \sqrt{\frac{E}{\rho}} \quad (20)$$

where  $k_B$  refers to the Boltzmann's constant,  $E$  is Young's modulus,  $\rho$  is the density of each perovskite crystal,  $N_A$  is Avogadro's number,  $M$  is the molecular weight, and  $n$  is the number of atoms. In this study, we have used the modification by Liu et al.<sup>149,150</sup> to the Clarke model through eq 21, which was proposed for the calculation of the minimum thermal

conductivity from DFT calculations of the elastic parameters ( $h$  is the Plank's constant)

$$\kappa_{\min} = \left\{ \frac{1}{3} \left[ 2 \left( \frac{1}{2 + 2\nu_H} \right)^{-3/2} + \left( \frac{1}{3 - 6\nu_H} + \frac{2}{3 + 3\nu_H} \right)^{-3/2} \right] \right\}^{-1/3} k_B N_A^{2/3} n^{2/3} \rho^{1/6} E_H^{-1/2} M^{2/3} \quad (21)$$

Another critical constant of thermal properties, the Debye temperature, is derived from eq 22<sup>153</sup>

$$\theta_D = \frac{h}{k_B} \left[ \frac{3n}{4\pi} \left( \frac{N_A \rho}{M} \right) \right]^{1/3} \nu_m \quad (22)$$

where  $\nu_m$ , the average sound velocity, is calculated by the eq 23

$$\nu_m = \left\{ \frac{1}{3} \left[ 2 \left( \frac{1}{2 + 2\nu_H} \right)^{-3/2} + \left( \frac{1}{3 - 6\nu_H} + \frac{2}{3 + 3\nu_H} \right)^{-3/2} \right] \right\}^{-1/3} \sqrt{\frac{E_H}{\rho}} \quad (23)$$

The calculated values of elastic constants for each of the studied materials with specific crystal structures are shown in Table 5.

The following stability criteria for each of the crystal phases have been demonstrated to be satisfied by the estimated values of these elastic constants.

BaTiO<sub>3</sub>, with a tetragonal crystal structure in the space group *P4mm* has six independent elastic constants, including  $C_{11}$ ,  $C_{12}$ ,  $C_{13}$ ,  $C_{33}$ ,  $C_{44}$ , and  $C_{66}$ . The values of these elastic constants satisfy the Born-Stability criteria for tetragonal crystal structures based on the below equations<sup>154</sup>

$$\begin{cases} C_{11} > |C_{12}|; C_{44} > 0 \\ 2C_{13}^2 < C_{33}(C_{11} + C_{12}) \\ 2C_{16}^2 < C_{66}(C_{11} - C_{12}) \end{cases}$$

CaTiO<sub>3</sub> with orthorhombic crystal structure with the space group *pnma* has 9 elastic constants  $C_{11}$ ,  $C_{12}$ ,  $C_{13}$ ,  $C_{22}$ ,  $C_{23}$ ,  $C_{33}$ ,  $C_{44}$ ,  $C_{55}$ , and  $C_{66}$ . The Born stability criteria for the orthorhombic system are well-known<sup>154</sup>

$$\begin{cases} C_{11} > 0; C_{44} > 0; C_{55} > 0; C_{66} > 0 \\ C_{11}C_{22} > C_{12}^2 \\ C_{11}C_{22}C_{33} + 2C_{12}C_{13}C_{23} - C_{11}C_{23}^2 - C_{22}C_{13}^2 - C_{33}C_{12}^2 > 0 \end{cases}$$

The trigonal structures of MgTiO<sub>3</sub> with space group  $\bar{R}3$  possesses 8 elastic constants of  $C_{11}$ ,  $C_{12}$ ,  $C_{13}$ ,  $C_{14}$ ,  $C_{15}$ ,  $C_{33}$ ,  $C_{44}$ , and  $C_{66}$ , while BeTiO<sub>3</sub> with *r3C* symmetry has 7 elastic constants  $C_{11}$ ,  $C_{12}$ ,  $C_{13}$ ,  $C_{14}$ ,  $C_{33}$ ,  $C_{44}$ , and  $C_{66}$ . In the case of a trigonal crystal, the assessment of mechanical stability requires three essential requirements, which could be described as follows<sup>155</sup>

$$\begin{cases} C_{11} - |C_{12}| = 2C_{66} > 0 \\ ((C_{11} - C_{66})C_{33} - C_{13}^2) > 0 \\ 2(C_{66}C_{44} - C_{14}^2) > 0 \end{cases}$$

The monoclinic structure of SrTiO<sub>3</sub> with space group *C2/m* is characterized by a total of 13 elastic constants, including  $C_{11}$ ,  $C_{12}$ ,  $C_{13}$ ,  $C_{15}$ ,  $C_{22}$ ,  $C_{23}$ ,  $C_{25}$ ,  $C_{33}$ ,  $C_{35}$ ,  $C_{44}$ ,  $C_{46}$ ,  $C_{55}$ , and  $C_{66}$ . Due to the complexity of the derived equations for the mechanical stability criterion of this crystal structure, they are provided in the supplementary file (see [Text S1](#)).<sup>156</sup>

The findings suggest that all compounds have some mechanical stability. This is because the calculated values for elastic stiffness constants satisfy the criteria for the mechanical stability of their corresponding crystal structures.

The main elastic parameters for studied perovskite oxides, including the bulk modulus, shear modulus, Young's modulus, Poisson's ratio, along with Minimum thermal conductivity and Debye temperature, plus the available results from other studies are listed in [Table 5](#). The magnitude of the indicated moduli for studied perovskite oxides follows the sequence of BeTiO<sub>3</sub> > CaTiO<sub>3</sub> > SrTiO<sub>3</sub> > MgTiO<sub>3</sub> > BaTiO<sub>3</sub>.

As can be observed, BeTiO<sub>3</sub> has the greatest bulk, Young's, and shear moduli (231.42, 305.47, and 119.32 GPa, respectively), whereas BaTiO<sub>3</sub> possesses the lowest values for the indicated moduli (129.23, 185.47, and 73.55 GPa, respectively). On the other hand, the bulk, Young's, and shear moduli of CaTiO<sub>3</sub> (186.32, 268.67, and 106.65 GPa, respectively) are higher than those of SrTiO<sub>3</sub> (181.24, 252.74, and 99.70 GPa, respectively) and MgTiO<sub>3</sub> (176.49, 228.87, and 89.13 GPa, respectively).

The degree of incompressibility is directly proportional to the magnitudes of the (*B*) and (*G*) values.<sup>157,158</sup> When three

mutually perpendicular stresses of equal intensity are applied to a structure, the ratio of direct stress to the corresponding volumetric strain is defined as the bulk modulus for the material. The volume strain is the ratio of the change in volume to the original volume when the pressure is applied uniformly over the entire material surface.<sup>159</sup> Therefore, the strength of a crystal could be evaluated by determining its bulk modulus. The structure will have a high compression strength and low compressibility if the bulk modulus is high.<sup>157</sup> Based on the data provided in [Table 5](#), BeTiO<sub>3</sub>, with the greatest (*B*), exhibits the greatest compression strength, while BaTiO<sub>3</sub>, with the lowest (*B*), demonstrates the highest compressibility. The shear modulus, which exhibits resistance to plastic deformation, is the ratio of the shear stress to the shear strain of material, where shear stress is the tangential force applied per unit of surface area. When an external force is applied tangentially to the surface of a body, while the opposite surface remains fixed, the body changes shape, but its volume remains unaltered. The face to which the force is applied is displaced in the direction of the applied force, which leads to shear strain within the material.<sup>160</sup> As can be seen in [Table 5](#), the greatest and lowest values of (*G*) is obtained for BeTiO<sub>3</sub> and BaTiO<sub>3</sub>, respectively. The ratio of the longitudinal stress to the longitudinal strain is defined as Young's modulus of elasticity. The change in length per unit length is the longitudinal strain, and the force acting per unit area of the cross-section of the material is the longitudinal stress.<sup>161</sup> The Young modulus illustrates how readily a substance may be stretched or deformed. The high value of the Young modulus proposed that this compound was stiff and could not be stretched or distorted readily.<sup>162</sup> The value of (*E*) for the investigated structures is in the order of BeTiO<sub>3</sub> > CaTiO<sub>3</sub> > SrTiO<sub>3</sub> > MgTiO<sub>3</sub> > BaTiO<sub>3</sub>. Poisson's ratio is an elastic constant as the ratio of lateral strain to longitudinal strain.<sup>163</sup> Poisson's ratio indicates the flexibility of the compound, and its ideal value ranges from 0 < (*ν*) < 0.5. The smaller the Poisson's ratio, the greater the plastic behavior, and vice versa, allowing us to conclude that the investigated compound was inherently elastic.<sup>158</sup> According to the information presented in [Table 5](#), BeTiO<sub>3</sub> and MgTiO<sub>3</sub> exhibit the greatest (*ν*) value of 0.28, while SrTiO<sub>3</sub> displays a (*ν*) value of 0.27. In contrast, CaTiO<sub>3</sub> and BaTiO<sub>3</sub> demonstrate the lowest value of 0.26.

An analysis has been conducted to determine the ductility and brittleness of these materials using several parameters, including the (*B*)/(*G*) ratio (Pugh ratio), and Poisson's ratio (*ν*). In contrast to brittle materials, which would alter the volume under stress, ductile materials would merely be deformed.<sup>158</sup> According to Pugh's criteria, a material is considered to exhibit ductile behavior if the ratio of (*B*)/(*G*) exceeds 1.75. Conversely, if this ratio is less than 1.75, the material is classified as brittle.<sup>157</sup> As indicated in [Table 5](#), the Pugh's ratio values for all the investigated compounds are ≥1.75. Consequently, they are all categorized as ductile materials, with the highest value observed in the case of MgTiO<sub>3</sub>. Poisson's ratio (*ν*) is another crucial factor for determining whether a material is ductile or brittle. Based on the Frantsevich rule, a material will exhibit a ductile nature if (*ν*) > 0.26 and a brittle behavior if (*ν*) < 0.26.<sup>164</sup> The displayed values of (*ν*) for the studied materials clearly demonstrate that all of them could be classified as ductile structures (see [Table 5](#)). In addition, (*ν*) is involved with the bonding characteristics of a substance. If (*ν*) is less than 0.10, the substance is covalent; between 0.25 and 0.33, it is ionic; beyond 0.33, it is

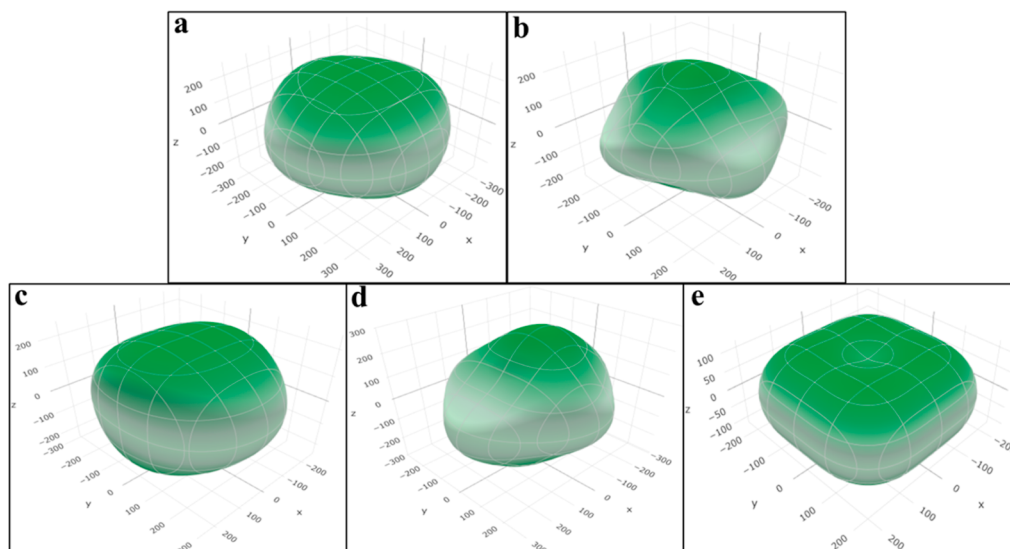


**Figure 11.** Calculated surface contours of spatial dependence of Young's modulus (in GPa) obtained from Hill approximation of the (a)  $\text{BeTiO}_3$ , (b)  $\text{MgTiO}_3$ , (c)  $\text{CaTiO}_3$ , (d)  $\text{SrTiO}_3$ , and (e)  $\text{BaTiO}_3$ .

metallic.<sup>165</sup> Therefore, based on this criterion, it can be concluded that the analyzed compounds should be categorized as ionic compounds.

The crystal elastic anisotropy factor indicated by  $A$  has significant implications in scientific study. To provide a quantitative assessment, the calculations ( $A = 2C_{44}/(C_{11} - C_{12})$ ) have been performed to determine the anisotropy factor. In the case when  $A$  is equal to 1, it could be inferred that the material has elastic isotropic characteristics. Conversely, if  $A$  deviates from this value, it signifies that the material possesses an anisotropic nature.<sup>166</sup>

As determined by the provided formula, the calculated  $A$  factor for all the studied compounds is below 1. This observation affirms the anisotropic nature of these compounds, as demonstrated in Table 5. Specifically, the  $A$  value for  $\text{CaTiO}_3$  stands at 0.98, which is the closest value to 1. This suggests that  $\text{CaTiO}_3$  exhibits characteristics that are relatively close to isotropic.

Surface contours of the spatially dependent Young's modulus from the Hill scheme for each crystal structure, showing the anisotropy for different perovskite materials, are illustrated in Figure 11, whereas the surface contours of spatial dependence of the shear modulus and Poisson's ratio of all structures are shown in Figures S2–S11.

The Debye temperature ( $\theta_D$ ), commonly referred to as the characteristic temperature, is a parameter significantly correlating with various physical properties, including the melting point, specific heat, Debye frequency, and elastic constants.<sup>166</sup> Elastic data can provide a precise method for predicting the Debye temperature. Additionally, a high Debye temperature is indicative of strong bonding within a material, owing to the connection between interatomic forces and the Debye temperature in solid material.<sup>167</sup> Based on the data presented in Table 5, all the investigated compounds exhibit high Debye temperature values exceeding 600, signifying strong bonding within these materials. In terms of this parameter, the compounds can be arranged as follows:  $\text{BeTiO}_3 > \text{CaTiO}_3 > \text{SrTiO}_3 > \text{MgTiO}_3 > \text{BaTiO}_3$ .

The minimum thermal conductivity of the perovskite oxides has been used to evaluate their thermal stability. The thermal

conductivity of a material is the number of Watts conducted per meter of material thickness per degree of the temperature differential between two sides. Generally, the lower the thermal conductivity of a material, the better, as it conducts less heat energy.<sup>168</sup> The minimum lattice thermal conductivities ( $\kappa_{\min}$ ) are 0.36, 0.28, 0.20, 0.19, and 0.18  $\text{W}\cdot\text{m}^{-1}\cdot\text{K}^{-1}$  for  $\text{CaTiO}_3$ ,  $\text{SrTiO}_3$ ,  $\text{BeTiO}_3$ ,  $\text{MgTiO}_3$ , and  $\text{BaTiO}_3$ , respectively (see Table 5). Therefore, the compounds with lower minimum thermal conductivity could improve the thermal stability of the cells upon their application in the structure of solar cells.

In conclusion, the performed elastic calculations confirmed the mechanical and thermal stability of  $\text{SrTiO}_3$  and  $\text{CaTiO}_3$ , reinforcing their suitability as ETL candidates.

These findings have been confirmed by other studies that have obtained elastic properties of titanium-based perovskite oxides.<sup>54,64,169</sup>

#### 4. CONCLUSION

The structural, optoelectronic, magnetic, thermal, and elastic properties of the  $\text{ATiO}_3$  ( $A = \text{Be, Mg, Ca, Sr, and Ba}$ ) perovskite oxides in different phases have been investigated using ab initio methods based on the density functional theory to gain insight into their potential application in polymer solar cells (PSCs) and perovskite solar cells (Per-SCs). The calculated tolerance factor confirms the stabilities of the compounds for each structure.

$\text{BeTiO}_3$ ,  $\text{MgTiO}_3$ ,  $\text{SrTiO}_3$ , and  $\text{BaTiO}_3$  show semiconductor behavior, resulting in indirect band gaps of 3.618, 4.852, 3.193, and 2.960 eV, respectively, whereas a direct band gap energy of 3.535 eV is calculated for the  $\text{CaTiO}_3$  compound. The PDOS results of the compounds reveal that O(2p) orbitals occupy the VB, whereas the contribution of Ti(3d) orbitals is prominent in the CBM. Considering the assessed electronic structures and the alignment of energy levels among diverse elements in the PSCs and Per-SCs, it is evident that all investigated compounds possess the capability to serve as electron transport layers (ETL) in the architecture of both devices. Notably,  $\text{BaTiO}_3$ ,  $\text{SrTiO}_3$ , and  $\text{CaTiO}_3$  exhibit the most favorable energy level alignment with commonly employed photoactive layers. Charge mobility results highlight that  $\text{SrTiO}_3$  and

CaTiO<sub>3</sub> demonstrate superior electron transport mobilities, positioning them as suitable choices for ETL. The minimal exciton binding energy observed in SrTiO<sub>3</sub> emphasizes its ease of separation and underscores its suitability for efficient carrier generation. These properties are expected to result in enhanced charge extraction and transportation from the photoactive layer to the ETL in the studied perovskite oxides, as evidenced by experimental results.

Furthermore, electronic structure along with optical findings, suggest that SrTiO<sub>3</sub> and CaTiO<sub>3</sub> should be the most fitting candidates for use as the ETL and TCE in solar cells. This is also attributed to their wide bandgap, higher transparency, low optical conductivity and absorptivity, minimal refractive index, and reflectivity of the light in the solar range.

Important elastic and thermal parameters, including the bulk modulus, shear modulus, Young's modulus, Poisson's ratio, Debye temperature, and minimum lattice thermal conductivities, were also calculated to evaluate the mechanical and thermal stability of the compounds. According to the results, all the investigated structures exhibit superior elastic and thermal properties, contributing to enhanced performance and stability of the solar cells.

In summary, we suggest that SrTiO<sub>3</sub> and CaTiO<sub>3</sub> compounds are suitable candidates for applications in CTLs and TCEs in PSCs and Per-SCs devices.

## ■ ASSOCIATED CONTENT

### Data Availability Statement

The raw/processed data required to reproduce these findings are available on request.

### Supporting Information

The Supporting Information is available free of charge at <https://pubs.acs.org/doi/10.1021/acs.jpcc.4c03863>.

Detailed information on the Energy level diagram of an inverted PSC and Per-SC, the born criteria for the mechanical stability of low symmetry monoclinic structure, and calculated surface contours of elastic modulus (PDF)

## ■ AUTHOR INFORMATION

### Corresponding Authors

Leila Naji – Department of Chemistry, AmirKabir University of Technology, 1591634311 Tehran, Iran; [orcid.org/0000-0003-1593-2751](https://orcid.org/0000-0003-1593-2751); Email: [leilanaji@aut.ac.ir](mailto:leilanaji@aut.ac.ir)

Saeedeh Sarabadani Tafreshi – Department of Chemistry, AmirKabir University of Technology, 1591634311 Tehran, Iran; School of Chemistry, University of Leeds, Leeds LS2 9JT, U.K.; [orcid.org/0000-0003-4130-437X](https://orcid.org/0000-0003-4130-437X); Email: [s.s.tafreshi@aut.ac.ir](mailto:s.s.tafreshi@aut.ac.ir), [S.SarabadaniTafreshi@leeds.ac.uk](mailto:S.SarabadaniTafreshi@leeds.ac.uk)

Nora H. de Leeuw – School of Chemistry, University of Leeds, Leeds LS2 9JT, U.K.; Department of Earth Sciences, Utrecht University, 3584 CB Utrecht, The Netherlands; [orcid.org/0000-0002-8271-0545](https://orcid.org/0000-0002-8271-0545); Email: [n.h.deleeuw@leeds.ac.uk](mailto:n.h.deleeuw@leeds.ac.uk)

### Authors

Shirzad Jouybar – Department of Chemistry, AmirKabir University of Technology, 1591634311 Tehran, Iran; [orcid.org/0009-0002-2664-7753](https://orcid.org/0009-0002-2664-7753)

Sayed Ahmad Mozaffari – Department of Chemical Technologies, Iranian Research Organization for Science and

Technology (IROST), 33535-111 Tehran, Iran;

[orcid.org/0000-0002-6334-0294](https://orcid.org/0000-0002-6334-0294)

Complete contact information is available at: <https://pubs.acs.org/10.1021/acs.jpcc.4c03863>

## Notes

The authors declare no competing financial interest.

## ■ ACKNOWLEDGMENTS

The authors would like to gratefully thank the Research Affairs Division of the Amirkabir University of Technology (AUT), Tehran, Iran, for their financial support. This work was supported by the UK Royal Society through an International Exchange Programme grant (IES\R3\223184). This work has used the computational facilities of the Advanced Research Computing at Cardiff (ARCCA) Division, Cardiff University, and HPC Wales. Via our membership of the UK's HEC Materials Chemistry Consortium, which is funded by EPSRC (EP/R029431), this work has also used the ARCHER2 UK National Supercomputing Service (<http://www.archer2.ac.uk>).

## ■ REFERENCES

- (1) Absike, H.; Baalla, N.; Attou, L.; Labrim, H.; Hartiti, B.; Ez-zahraouy, H. Theoretical investigations of structural, electronic, optical and thermoelectric properties of oxide halide perovskite ACoO<sub>3</sub> (A = Nd, Pr or La). *Solid State Commun.* **2022**, *345*, 114684.
- (2) Jouybar, S.; Naji, L.; Mozaffari, S. A.; Sarabadani Tafreshi, S.; de Leeuw, N. H. Electrochemically Engineered Lanthanum Nickelate as a Promising Transparent Hole-Transport Layer for Bulk Heterojunction Polymer Solar Cells: An Experimental and DFT Study. *ACS Appl. Energy Mater.* **2024**, *7* (4), 1647–1665.
- (3) Mahapatra, A.; Prochowicz, D.; Tavakoli, M. M.; Trivedi, S.; Kumar, P.; Yadav, P. A review of aspects of additive engineering in perovskite solar cells. *J. Mater. Chem. A* **2020**, *8* (1), 27–54.
- (4) Zhu, K.; Chen, Y.; Wang, Y.; Feng, M.; Zhao, Y. Progress of Solution-Processed Metal Oxides as Charge Transport Layers towards Efficient and Stable Perovskite Solar Cells and Modules. *Mater. Today Nano* **2022**, *20*, 100252.
- (5) Yin, Z.; Wei, J.; Zheng, Q. Interfacial materials for organic solar cells: recent advances and perspectives. *Advanced Science* **2016**, *3* (8), 1500362.
- (6) Anrango-Camacho, C.; Pavón-Ipiales, K.; Frontana-Urbe, B. A.; Palma-Cando, A. Recent advances in hole-transporting layers for organic solar cells. *Nanomaterials* **2022**, *12* (3), 443.
- (7) Fan, X. Doping and Design of Flexible Transparent Electrodes for High-Performance Flexible Organic Solar Cells: Recent Advances and Perspectives. *Adv. Funct. Mater.* **2021**, *31* (8), 2009399.
- (8) Jouybar, S.; Yazdani, F. Synthesis of Magnetite Nanoparticles Under UV/IR Irradiation: Investigation of Effects on the Properties. *Nanosci. Nanotechnol.* **2018**, *8* (2), 289–296.
- (9) Jouybar, S.; Naji, L.; Mozaffari, S. A.; Sarabadani Tafreshi, S. In Situ Electrochemical Cobalt Doping in Perovskite-Structured Lanthanum Nickelate Thin Film Toward Energy Conversion Enhancement of Polymer Solar Cells. *ACS Appl. Mater. Interfaces* **2024**, *16* (25), 32857–32873.
- (10) Wang, J.; Liu, Y.; Chen, X.; Chen, C.; Chen, P.; Wang, Z.; Duan, Y. Functional metal oxides in perovskite solar cells. *ChemPhysChem* **2019**, *20* (20), 2580–2586.
- (11) Liu, H.; Huang, Z.; Wei, S.; Zheng, L.; Xiao, L.; Gong, Q. Nano-structured electron transporting materials for perovskite solar cells. *Nanoscale* **2016**, *8* (12), 6209–6221.
- (12) Mahmood, K.; Khalid, A.; Nawaz, F.; Mehran, M. T. Low-temperature electrospray-processed SnO<sub>2</sub> nanosheets as an electron transporting layer for stable and high-efficiency perovskite solar cells. *J. Colloid Interface Sci.* **2018**, *532*, 387–394.

- (13) Si, H.; Liao, Q.; Zhang, Z.; Li, Y.; Yang, X.; Zhang, G.; Kang, Z.; Zhang, Y. An innovative design of perovskite solar cells with Al<sub>2</sub>O<sub>3</sub> inserting at ZnO/perovskite interface for improving the performance and stability. *Nano Energy* **2016**, *22*, 223–231.
- (14) Pisoni, S.; Fu, F.; Feurer, T.; Makha, M.; Bissig, B.; Nishiwaki, S.; Tiwari, A. N.; Buecheler, S. Flexible NIR-transparent perovskite solar cells for all-thin-film tandem photovoltaic devices. *J. Mater. Chem. A* **2017**, *5* (26), 13639–13647.
- (15) Liang, F.; Lin, Y.; He, Z.; Chen, W.; Zhu, Y.; Chen, T.; Liang, L.; Ma, S.; Wu, Y.; Tu, B.; et al. Promising ITO-free perovskite solar cells with WO<sub>3</sub>-Ag-SnO<sub>2</sub> as transparent conductive oxide. *J. Mater. Chem. A* **2018**, *6* (40), 19330–19337.
- (16) Han, G. S.; Chung, H. S.; Kim, B. J.; Kim, D. H.; Lee, J. W.; Swain, B. S.; Mahmood, K.; Yoo, J. S.; Park, N.-G.; Lee, J. H.; et al. Retarding charge recombination in perovskite solar cells using ultrathin MgO-coated TiO<sub>2</sub> nanoparticulate films. *J. Mater. Chem. A* **2015**, *3* (17), 9160–9164.
- (17) Xu, X.; Liu, Z.; Zuo, Z.; Zhang, M.; Zhao, Z.; Shen, Y.; Zhou, H.; Chen, Q.; Yang, Y.; Wang, M. Hole selective NiO contact for efficient perovskite solar cells with carbon electrode. *Nano Lett.* **2015**, *15* (4), 2402–2408.
- (18) Gershon, T. Metal oxide applications in organic-based photovoltaics. *Mater. Sci. Technol.* **2011**, *27* (9), 1357–1371.
- (19) Gonzalez-Valls, I.; Lira-Cantu, M. Vertically-aligned nanostructures of ZnO for excitonic solar cells: a review. *Energy Environ. Sci.* **2009**, *2* (1), 19–34.
- (20) Abbasi, A.; Sardroodi, J. J. Molecular design of O<sub>3</sub> and NO<sub>2</sub> sensor devices based on a novel heterostructured N-doped TiO<sub>2</sub>/ZnO nanocomposite: a van der Waals corrected DFT study. *J. Nanostruct. Chem.* **2017**, *7*, 345–358.
- (21) Haque, M. A.; Sheikh, A. D.; Guan, X.; Wu, T. Metal oxides as efficient charge transporters in perovskite solar cells. *Adv. Energy Mater.* **2017**, *7* (20), 1602803.
- (22) Rowell, M. W.; McGehee, M. D. Transparent electrode requirements for thin film solar cell modules. *Energy Environ. Sci.* **2011**, *4* (1), 131–134.
- (23) Nuraje, N.; Asmatulu, R.; Kudaibergenov, S. Metal oxide-based functional materials for solar energy conversion: a review. *Curr. Inorg. Chem.* **2012**, *2* (2), 124–146.
- (24) Shin, S.; Lee, S.; Seok, S. I. Exploring wide bandgap metal oxides for perovskite solar cells. *APL Mater.* **2019**, *7* (2), 022401.
- (25) Rizwan, M.; Khadija, Z.; Mahmood, T.; Gillani, S.; Khan, M. I. Alteration impact of electronic properties of c-SrTiO<sub>3</sub> on optical response due to Ca inclusion: A DFT study. *Phys. B* **2021**, *602*, 412553.
- (26) Travis, W.; Glover, E.; Bronstein, H.; Scanlon, D.; Palgrave, R. On the application of the tolerance factor to inorganic and hybrid halide perovskites: a revised system. *Chem. Sci.* **2016**, *7* (7), 4548–4556.
- (27) Warner, T. E. *Synthesis, properties and mineralogy of important inorganic materials*; John Wiley & Sons, 2012.
- (28) Bano, A.; Gaur, N. Effect of SrO termination on electron transport of MoS<sub>2</sub>/SrTiO<sub>3</sub> heterostructure: A DFT approach. *Appl. Surf. Sci.* **2019**, *487*, 1403–1408.
- (29) Boubchir, M.; Aourag, H. Materials genome project: Mining the ionic conductivity in oxide perovskites. *J. Mater. Sci. Eng. B* **2021**, *267*, 114984.
- (30) Atta, N. F.; Galal, A.; El-Ads, E. H. Perovskite nanomaterials-synthesis, characterization, and applications. In *Perovskite Materials-Synthesis, Characterisation, Properties, and Applications*; InTech Open, 2016; pp 107–151.
- (31) Castelli, I. E.; Olsen, T.; Datta, S.; Landis, D. D.; Dahl, S.; Thygesen, K. S.; Jacobsen, K. W. Computational screening of perovskite metal oxides for optimal solar light capture. *Energy Environ. Sci.* **2012**, *5* (2), 5814–5819.
- (32) Castelli, I. E.; Landis, D. D.; Thygesen, K. S.; Dahl, S.; Chorkendorff, I.; Jaramillo, T. F.; Jacobsen, K. W. New cubic perovskites for one-and two-photon water splitting using the computational materials repository. *Energy Environ. Sci.* **2012**, *5* (10), 9034–9043.
- (33) Djellabi, R.; Ordonez, M. F.; Conte, F.; Falletta, E.; Bianchi, C. L.; Rossetti, I. A review of advances in multifunctional XTiO<sub>3</sub> perovskite-type oxides as piezo-photocatalysts for environmental remediation and energy production. *J. Hazard. Mater.* **2022**, *421*, 126792.
- (34) Kucharczyk, B.; Okal, J.; Tylus, W.; Winiarski, J.; Szczygiel, B. The effect of the calcination temperature of LaFeO<sub>3</sub> precursors on the properties and catalytic activity of perovskite in methane oxidation. *Ceram. Int.* **2019**, *45* (2), 2779–2788.
- (35) Rached, H.; Bendaoudia, S.; Rached, D. Investigation of Iron-based double perovskite oxides on the magnetic phase stability, mechanical, electronic and optical properties via first-principles calculation. *Mater. Chem. Phys.* **2017**, *193*, 453–469.
- (36) Gao, W.; Zhu, Y.; Wang, Y.; Yuan, G.; Liu, J.-M. A review of flexible perovskite oxide ferroelectric films and their application. *J. Mater.* **2020**, *6* (1), 1–16.
- (37) Guo, Y.; Ma, L.; Mao, K.; Ju, M.; Bai, Y.; Zhao, J.; Zeng, X. C. Eighteen functional monolayer metal oxides: wide bandgap semiconductors with superior oxidation resistance and ultrahigh carrier mobility. *Nanoscale Horiz.* **2019**, *4* (3), 592–600.
- (38) Zhu, L.; Shao, Z.; Ye, J.; Zhang, X.; Pan, X.; Dai, S. Mesoporous BaSnO<sub>3</sub> layer based perovskite solar cells. *Chem. Commun.* **2016**, *52* (5), 970–973.
- (39) Shin, S. S.; Kim, J. S.; Suk, J. H.; Lee, K. D.; Kim, D. W.; Park, J. H.; Cho, I. S.; Hong, K. S.; Kim, J. Y. Improved quantum efficiency of highly efficient perovskite BaSnO<sub>3</sub>-based dye-sensitized solar cells. *ACS Nano* **2013**, *7* (2), 1027–1035.
- (40) Rajamanickam, N.; Soundarajan, P.; Vendra, V. K.; Jasinski, J. B.; Sunkara, M. K.; Ramachandran, K. Efficiency enhancement of cubic perovskite BaSnO<sub>3</sub> nanostructures based dye sensitized solar cells. *Phys. Chem. Chem. Phys.* **2016**, *18* (12), 8468–8478.
- (41) Rajamanickam, N.; Soundarajan, P.; Jayakumar, K.; Ramachandran, K. Improve the power conversion efficiency of perovskite BaSnO<sub>3</sub> nanostructures based dye-sensitized solar cells by Fe doping. *Sol. Energy Mater. Sol. Cells* **2017**, *166*, 69–77.
- (42) Neophytou, M.; De Bastiani, M.; Gasparini, N.; Aydin, E.; Ugur, E.; Seitkhan, A.; Moruzzi, F.; Choie, Y.; Ramadan, A. J.; Troughton, J. R.; et al. Enhancing the charge extraction and stability of perovskite solar cells using strontium titanate (SrTiO<sub>3</sub>) electron transport layer. *ACS Appl. Energy Mater.* **2019**, *2* (11), 8090–8097.
- (43) Okamoto, Y.; Fukui, R.; Fukazawa, M.; Suzuki, Y. SrTiO<sub>3</sub>/TiO<sub>2</sub> composite electron transport layer for perovskite solar cells. *Mater. Lett.* **2017**, *187*, 111–113.
- (44) Wang, C.; Tang, Y.; Hu, Y.; Huang, L.; Fu, J.; Jin, J.; Shi, W.; Wang, L.; Yang, W. Graphene/SrTiO<sub>3</sub> nanocomposites used as an effective electron-transporting layer for high-performance perovskite solar cells. *RSC Adv.* **2015**, *5* (64), 52041–52047.
- (45) Kim, D. W.; Shin, S. S.; Lee, S.; Cho, I. S.; Kim, D. H.; Lee, C. W.; Jung, H. S.; Hong, K. S. BaSnO<sub>3</sub> perovskite nanoparticles for high efficiency dye-sensitized solar cells. *ChemSusChem* **2013**, *6* (3), 449–454.
- (46) Roy, A.; Das, P. P.; Selvaraj, P.; Sundaram, S.; Devi, P. S. Perforated BaSnO<sub>3</sub> nanorods exhibiting enhanced efficiency in dye sensitized solar cells. *ACS Sustain. Chem. Eng.* **2018**, *6* (3), 3299–3310.
- (47) Gholamrezaei, S.; Salavati Niasari, M.; Dadkhah, M.; Sarkhosh, B. New modified sol-gel method for preparation SrTiO<sub>3</sub> nanostructures and their application in dye-sensitized solar cells. *J. Mater. Sci.: Mater. Electron.* **2016**, *27* (1), 118–125.
- (48) Okamoto, Y.; Suzuki, Y. Perovskite-type SrTiO<sub>3</sub>, CaTiO<sub>3</sub> and BaTiO<sub>3</sub> porous film electrodes for dye-sensitized solar cells. *J. Ceram. Soc. Jpn.* **2014**, *122* (1428), 728–731.
- (49) Shang, Q.; Yu, J.; Hu, R.; Liu, Z.; Cheng, J.; Li, Y.; Shai, X.; Huo, M.-m.; Yang, X.; Li, L. Enhanced charge transport in conventional polymer solar cells with a perovskite-type LaNiO<sub>3</sub> layer. *ACS Appl. Mater. Interfaces* **2020**, *12* (11), 13051–13060.

- (50) Nazir, S.; Noor, N.; Afzal, Q.; Mahmood, A. Pressure-Induced Thermodynamic and Opto-Electronic Behavior of  $\text{BaTiO}_3$  Perovskite: A DFT Investigation. *J. Electron. Mater.* **2020**, *49* (5), 3072–3079.
- (51) Rizwan, M.; Zeba, I.; Zeba, I.; Shakil, M.; Gillani, S.; Usman, Z. Electronic, structural and optical properties of  $\text{BaTiO}_3$  doped with lanthanum (La): Insight from DFT calculation. *Optik* **2020**, *211*, 164611.
- (52) Li, Y.; Niu, S.; Wang, J.; Zhou, W.; Wang, Y.; Han, K.; Lu, C. Mesoporous  $\text{SrTiO}_3$  perovskite as a heterogeneous catalyst for biodiesel production: Experimental and DFT studies. *Renewable Energy* **2022**, *184*, 164–175.
- (53) Rusevich, L. L.; Zvejnieks, G.; Kotomin, E. A.; Kržmanc, M. M.; Meden, A.; Kunej, S. p.; Vlaicu, I. D. Theoretical and experimental study of (Ba, Sr)  $\text{TiO}_3$  perovskite solid solutions and  $\text{BaTiO}_3/\text{SrTiO}_3$  heterostructures. *J. Phys. Chem. C* **2019**, *123* (4), 2031–2036.
- (54) Adewale, A. A.; Chik, A.; Adam, T.; Yusuff, O. K.; Ayinde, S. A.; Sanusi, Y. K. First principles calculations of structural, electronic, mechanical and thermoelectric properties of cubic  $\text{ATiO}_3$  (A = Be, Mg, Ca, Sr and Ba) perovskite oxide. *Comput. Condens. Matter* **2021**, *28*, No. e00562.
- (55) Yun, J.; Zhang, Z.; Zhang, F.; Zhao, W. Study of electronic structure and conductivity of Nb-doped  $\text{SrTiO}_3$  by density function theory. In *2008 3rd IEEE International Conference on Nano/Micro Engineered and Molecular Systems*, 2008; IEEE: pp 664–668.
- (56) Akbay, T.; Staykov, A.; Druce, J.; Téllez, H.; Ishihara, T.; Kilner, J. A. The interaction of molecular oxygen on  $\text{LaO}$  terminated surfaces of  $\text{La}_2\text{NiO}_4$ . *J. Mater. Chem. A* **2016**, *4* (34), 13113–13124.
- (57) Li, X.; Li, P.; Wu, Z.; Luo, D.; Yu, H.-Y.; Lu, Z.-H. Review and perspective of materials for flexible solar cells. *Mater. Rep.: Energy* **2021**, *1* (1), 100001.
- (58) Forozaandeh, A.; Pourmadadi, M.; SalarAmoli, H.; Abdouss, M. Aptamer-enabled electrochemical bioplatfrom utilizing surface-modified  $\text{g-C}_3\text{N}_4/\text{MoS}_2/\text{PANI}$  nanocomposite for detection of CA125 biomarker. *Sensing and Bio-Sensing Research* **2024**, *45*, 100669.
- (59) Xu, Y.; Lin, Z.; Wei, W.; Hao, Y.; Liu, S.; Ouyang, J.; Chang, J. Recent Progress of Electrode Materials for Flexible Perovskite Solar Cells. *Nano-Micro Lett.* **2022**, *14* (1), 117.
- (60) Rizwan, M.; Shahid, A.; Mahmood, T.; Zafar, A. A.; Aslam, I.; Adnan, N.; Hussain, T.; Jin, H.; Cao, C. Effect of magnesium on structural and optical properties of  $\text{CaTiO}_3$ : a DFT study. *Phys. B* **2019**, *568*, 88–91.
- (61) Tariq, S.; Ahmed, A.; Saad, S.; Tariq, S. Structural, electronic and elastic properties of the cubic  $\text{CaTiO}_3$  under pressure: A DFT study. *AIP Adv.* **2015**, *5* (7), 077111.
- (62) Wang, Y.; Lian, W.; Liu, Y. Electronic structure and optical properties in alkaline-earth metals (A = Mg, Ca, Ba) and Ir co-doped  $\text{SrTiO}_3$ : A DFT+U investigation. *Optik* **2021**, *228*, 166128.
- (63) Rizwan, M.; Ali, A.; Usman, Z.; Khalid, N.; Jin, H.; Cao, C. Structural, electronic and optical properties of copper-doped  $\text{SrTiO}_3$  perovskite: A DFT study. *Phys. B* **2019**, *552*, 52–57.
- (64) Lebedev, A. I. Ab initio calculations of phonon spectra in  $\text{ATiO}_3$  perovskite crystals (A = Ca, Sr, Ba, Ra, Cd, Zn, Mg, Ge, Sn, Pb). *Phys. Solid State* **2009**, *51* (2), 362–372.
- (65) Evarestov, R. A.; Bandura, A. V. First-principles calculations on the four phases of  $\text{BaTiO}_3$ . *J. Comput. Chem.* **2012**, *33* (11), 1123–1130.
- (66) Sokolov, M.; Eglitis, R.; Piskunov, S.; Zhukovskii, Y. F. Ab initio hybrid DFT calculations of  $\text{BaTiO}_3$  bulk and  $\text{BaO}$ -terminated (001) surface F-centers. *Int. J. Mod. Phys. B* **2017**, *31* (31), 1750251.
- (67) Kresse, G.; Furthmüller, J. Efficiency of ab-initio total energy calculations for metals and semiconductors using a plane-wave basis set. *Comput. Mater. Sci.* **1996**, *6* (1), 15–50.
- (68) Demir, S.; Torkashvand, M.; Jouybar, S.; Nikfarjam, Z.; Zargari, F.; Tafreshi, S. S.; Tekin, A. Hydrogen Storage in Trimetallic Borohydrides: a Crystal Structure Prediction and Ab Initio Molecular Dynamics Simulations Study. *J. Phys. Chem. C* **2023**, *127* (39), 19344–19355.
- (69) Jouybar, S.; Naji, L.; Sarabadani Tafreshi, S.; de Leeuw, N. H. A Density Functional Theory Study of the Physico-Chemical Properties of Alkali Metal Titanate Perovskites for Solar Cell Applications. *Molecules* **2024**, *29*, 3355.
- (70) Hosseini, S. M.; Soltanabadi, A.; Abdouss, M.; Mazinani, S. Investigating the structure of the product of graphene oxide reaction with folic acid and chitosan: density functional theory calculations. *J. Biomol. Struct. Dyn.* **2022**, *40* (24), 14146–14159.
- (71) Krukau, A.; Vydrov, O.; Izmaylov, A.; Scuseria, G. Influence of the exchange screening parameter on the performance of screened hybrid functionals. *J. Chem. Phys.* **2006**, *125*, 224106.
- (72) Logsdail, A. J.; Scanlon, D. O.; Catlow, C. R. A.; Sokol, A. A. Bulk ionization potentials and band alignments from three-dimensional periodic calculations as demonstrated on rocksalt oxides. *Phys. Rev. B* **2014**, *90* (15), 155106.
- (73) Wang, V.; Xu, N.; Liu, J.-C.; Tang, G.; Geng, W.-T. VASPKIT: A user-friendly interface facilitating high-throughput computing and analysis using VASP code. *Comput. Phys. Commun.* **2021**, *267*, 108033.
- (74) Gaillac, R.; Pullumbi, P.; Coudert, F.-X. ELATE: an open-source online application for analysis and visualization of elastic tensors. *J. Phys.: Condens. Matter* **2016**, *28* (27), 275201.
- (75) Kirklin, S.; Saal, J. E.; Meredig, B.; Thompson, A.; Doak, J. W.; Aykol, M.; Rühl, S.; Wolverton, C. The Open Quantum Materials Database (OQMD): assessing the accuracy of DFT formation energies. *npj Comput. Mater.* **2015**, *1* (1), 15010.
- (76) Goodenough, J. B. Electronic and ionic transport properties and other physical aspects of perovskites. *Rep. Prog. Phys.* **2004**, *67* (11), 1915–1993.
- (77) Maddah, H. A.; Berry, V.; Behura, S. K. Cuboctahedral stability in Titanium halide perovskites via machine learning. *Comput. Mater. Sci.* **2020**, *173*, 109415.
- (78) Saal, J. E.; Kirklin, S.; Aykol, M.; Meredig, B.; Wolverton, C. Materials Design and Discovery with High-Throughput Density Functional Theory: The Open Quantum Materials Database (OQMD). *JOM* **2013**, *65* (11), 1501–1509.
- (79) Jain, A.; Ong, S.; Hautier, G.; Chen, W.; Richards, W.; Dacek, S.; Cholia, S.; Gunter, D.; Skinner, D.; Ceder, G.; Persson, K. Commentary: The Materials Project: A materials genome approach to accelerating materials innovation. *APL Mater.* **2013**, *1*, 011002.
- (80) Cho, N. W.; Sung, K.; Chang, S. Synthesis and crystal structure refinement of  $(1-x)\text{CaTiO}_3(x)(\text{La}_1/3\text{Nd}_1/3)\text{TiO}_3$ . *RIST Yongu Nonmun* **1998**, *12*, 116.
- (81) Kwei, G.; Lawson, A. C.; Billinge, S. J. L.; Cheong, S. W. Structures of the ferroelectric phases of barium titanate. *W. Cheong. J. Phys. Chem* **1993**, *97*, 2368–2377.
- (82) Mohamad Noh, M. F.; Teh, C. H.; Daik, R.; Lim, E. L.; Yap, C. C.; Ibrahim, M. A.; Ahmad Ludin, N.; Mohd Yusoff, A. R. b.; Jang, J.; Mat Teridi, M. A. The architecture of the electron transport layer for a perovskite solar cell. *J. Mater. Chem. C* **2018**, *6* (4), 682–712.
- (83) Zhang, H.; Chen, G.; He, X.; Xu, J. Electronic structure and photocatalytic properties of Ag-La codoped  $\text{CaTiO}_3$ . *J. Alloys Compd.* **2012**, *516*, 91–95.
- (84) Lv, H.; Gao, H.; Yang, Y.; Liu, L. Density functional theory (DFT) investigation on the structure and electronic properties of the cubic perovskite  $\text{PbTiO}_3$ . *Appl. Catal., A* **2011**, *404* (1), 54–58.
- (85) Wen, H.; Luo, X. Tuning Bandgaps of Mixed Halide and Oxide Perovskites  $\text{CsSnX}_3$  (X = Cl, I), and  $\text{SrBO}_3$  (B = Rh, Ti). *Appl. Sci.* **2021**, *11*, 6862.
- (86) Ribeiro, R. A. P.; Camilo, A.; de Lazaro, S. R. Electronic structure and magnetism of new ilmenite compounds for spintronic devices:  $\text{FeBO}_3$  (B = Ti, Hf, Zr, Si, Ge, Sn). *J. Magn. Magn. Mater.* **2015**, *394*, 463–469.
- (87) Khan, S.; Humera, N.; Niaz, S.; Riaz, S.; Atiq, S.; Naseem, S. Simultaneous normal - Anomalous dielectric dispersion and room temperature ferroelectricity in CBD perovskite  $\text{BaTiO}_3$  thin films. *J. Mater. Res. Technol.* **2020**, *9* (5), 11439–11452.
- (88) Fujisawa, J.-i.; Eda, T.; Hanaya, M. Comparative study of conduction-band and valence-band edges of  $\text{TiO}_2$ ,  $\text{SrTiO}_3$ , and

- BaTiO<sub>3</sub> by ionization potential measurements. *Chem. Phys. Lett.* **2017**, *685*, 23–26.
- (89) Siebenhofer, M.; Viernstein, A.; Morgenbesser, M.; Fleig, J.; Kubicek, M. Photoinduced Electronic and Ionic Effects in Strontium Titanate. *Mater. Adv.* **2021**, *2*, 7583–7619.
- (90) Issam, D.; Achehboune, M.; Boukhoubza, I.; Hatel, R.; El Adnani, Z.; Rezzouk, A. Investigation of the crystal structure, electronic and optical properties of Cr-doped BaTiO<sub>3</sub> on the Ti site using first principles calculations. *J. Phys. Chem. Solids* **2023**, *175*, 111209.
- (91) Negishi, M.; Fujiwara, K.; Tsukazaki, A. Formation of ilmenite-type single-crystalline MgTiO<sub>3</sub> thin films by pulsed-laser deposition. *AIP Adv.* **2021**, *11*, 125125.
- (92) Boudali, A.; Abada, A.; Driss Khodja, M.; Amrani, B.; Amara, K.; Driss Khodja, F.; Elias, A. Calculation of structural, elastic, electronic, and thermal properties of orthorhombic CaTiO<sub>3</sub>. *Phys. B* **2010**, *405* (18), 3879–3884.
- (93) Chueh, C.-C.; Li, C.-Z.; Jen, A. K. Y. Recent progress and perspective in solution-processed Interfacial materials for efficient and stable polymer and organometal perovskite solar cells. *Energy Environ. Sci.* **2015**, *8* (4), 1160–1189.
- (94) Chen, J.; Park, N.-G. Materials and Methods for Interface Engineering toward Stable and Efficient Perovskite Solar Cells. *ACS Energy Lett.* **2020**, *5* (8), 2742–2786.
- (95) Pascual-San-José, E.; Rodríguez-Martínez, X.; Adel-Abdelaleim, R.; Stella, M.; Martínez-Ferrero, E.; Campoy-Quiles, M. Blade coated P3HT:non-fullerene acceptor solar cells: a high-throughput parameter study with a focus on up-scalability. *J. Mater. Chem. A* **2019**, *7*, 20369–20382.
- (96) Zhang, K.-N.; Niu, M.-S.; Jiang, Z.-N.; Chen, Z.; Wang, T.; Wei, M.-M.; Qin, C.-C.; Feng, L.; Qin, W.; so, S.; Hao, X.-T. Multiple Temporal-Scale Photocarrier Dynamics Induced by Synergistic Effects of Fluorination and Chlorination in Highly Efficient Nonfullerene Organic Solar Cells. *Sol. RRL* **2020**, *4*, 2070046.
- (97) Hashemi, D.; Ma, X.; Ansari, R.; Kim, J.; Kieffer, J. Design principles for the energy level tuning in donor/acceptor conjugated polymers. *Phys. Chem. Chem. Phys.* **2019**, *21* (2), 789–799.
- (98) Joseph, S.; Ravva, M. K.; Davis, B.; Thomas, S.; Kalarikkal, N. Theoretical Study on Understanding the Effects of Core Structure and Energy Level Tuning on Efficiency of Nonfullerene Acceptors in Organic Solar Cells. *Adv. Theory Simul.* **2021**, *4*, 2100019.
- (99) Hassan, T.; Adnan, M.; Hussain, R.; Hussain, F.; Khan, M. U. Molecular engineering of Pyran-fused acceptor–donor–acceptor-type non-fullerene acceptors for highly efficient organic solar cells—A density functional theory approach. *J. Phys. Org. Chem.* **2023**, *36*, No. e4507.
- (100) Bera, A.; Wu, K.; Sheikh, A.; Alarousu, E.; Mohammed, O. F.; Wu, T. Perovskite Oxide SrTiO<sub>3</sub> as an Efficient Electron Transporter for Hybrid Perovskite Solar Cells. *J. Phys. Chem. C* **2014**, *118* (49), 28494–28501.
- (101) Gupta, A.; Srivastava, V.; Yadav, S.; Lohia, P.; Dwivedi, D. K.; Umar, A.; Mahmoud, M. Performance Enhancement of Perovskite Solar Cell Using SrTiO<sub>3</sub> as Electron Transport Layer. *J. Nanoelectron. Optoelectron.* **2023**, *18*, 452–458.
- (102) Lan, J.-L.; Liang, Z.; Yang, Y.-H.; Ohuchi, F. S.; Jenekhe, S. A.; Cao, G. The effect of SrTiO<sub>3</sub>:ZnO as cathodic buffer layer for inverted polymer solar cells. *Nano Energy* **2014**, *4*, 140–149.
- (103) Hu, Y.; Wang, C.; Tang, Y.; Huang, L.; Fu, J.; Shi, W.; Wang, L.; Yang, W. Three-dimensional self-branching anatase TiO<sub>2</sub> nanorods with the improved carrier collection for SrTiO<sub>3</sub>-based perovskite solar cells. *J. Alloys Compd.* **2016**, *679*, 32–38.
- (104) Liu, D.; Kelly, T. L. Perovskite solar cells with a planar heterojunction structure prepared using room-temperature solution processing techniques. *Nat. Photonics* **2014**, *8* (2), 133–138.
- (105) Rao, H. S.; Chen, B. X.; Li, W. G.; Xu, Y. F.; Chen, H. Y.; Kuang, D. B.; Su, C. Y. Improving the extraction of photogenerated electrons with SnO<sub>2</sub> nanocolloids for efficient planar perovskite solar cells. *Adv. Funct. Mater.* **2015**, *25* (46), 7200–7207.
- (106) Yang, D.; Yang, R.; Wang, K.; Wu, C.; Zhu, X.; Feng, J.; Ren, X.; Fang, G.; Priya, S.; Liu, S. High efficiency planar-type perovskite solar cells with negligible hysteresis using EDTA-complexed SnO<sub>2</sub>. *Nat. Commun.* **2018**, *9* (1), 3239.
- (107) Li, S.; Zhang, P.; Wang, Y.; Sarvari, H.; Liu, D.; Wu, J.; Yang, Y.; Wang, Z.; Chen, Z. D. Interface engineering of high efficiency perovskite solar cells based on ZnO nanorods using atomic layer deposition. *Nano Res.* **2017**, *10* (3), 1092–1103.
- (108) Xiong, L.; Qin, M.; Chen, C.; Wen, J.; Yang, G.; Guo, Y.; Ma, J.; Zhang, Q.; Qin, P.; Li, S.; et al. Fully High-Temperature-Processed SnO<sub>2</sub> as Blocking Layer and Scaffold for Efficient, Stable, and Hysteresis-Free Mesoporous Perovskite Solar Cells. *Adv. Funct. Mater.* **2018**, *28*, 1706276.
- (109) Kaasbjerg, K.; Thygesen, K.; Jauho, A.-P. Acoustic phonon limited mobility in two-dimensional semiconductors: Deformation potential and piezoelectric scattering in monolayer MoS<sub>2</sub> from first principles. *Phys. Rev. B* **2013**, *87*, 235312.
- (110) Kaasbjerg, K.; Thygesen, K. S.; Jacobsen, K. W. Phonon-limited mobility in n-type single-layer MoS<sub>2</sub> from first principles. *Phys. Rev. B* **2012**, *85* (11), 115317.
- (111) Bardeen, J.; Shockley, W. Deformation potentials and mobilities in non-polar crystals. *Phys. Rev.* **1950**, *80* (1), 72–80.
- (112) Murphy-Armando, F.; Fahy, S. First-principles calculation of carrier-phonon scattering in n-type Si<sub>1-x</sub>Ge<sub>x</sub> alloys. *Phys. Rev. B* **2008**, *78*, 035202.
- (113) Tiwana, P.; Docampo, P.; Johnston, M. B.; Snaith, H. J.; Herz, L. M. Electron Mobility and Injection Dynamics in Mesoporous ZnO, SnO<sub>2</sub>, and TiO<sub>2</sub> Films Used in Dye-Sensitized Solar Cells. *ACS Nano* **2011**, *5* (6), 5158–5166.
- (114) Ying, Y.; Luo, X.; Huang, H. Pressure-Induced Topological Nontrivial Phase and Tunable Optical Properties in All-Inorganic Halide Perovskites. *J. Phys. Chem. C* **2018**, *122* (31), 17718–17725.
- (115) Xie, M.; Zhang, S.; Cai, B.; Huang, Y.; Zou, Y.; Guo, B.; Gu, Y.; Zeng, H. A promising two-dimensional solar cell donor: Black arsenic-phosphorus monolayer with 1.54eV direct bandgap and mobility exceeding 14,000cm<sup>2</sup>V<sup>-1</sup>s<sup>-1</sup>. *Nano Energy* **2016**, *28*, 433–439.
- (116) Jong, U.-G.; Yu, C.-J.; Kye, Y.-H.; Hong, S.-N.; Kim, H.-G. Manifestation of the thermoelectric properties in Ge-based halide perovskites. *Phys. Rev. Mater.* **2020**, *4*, 075403.
- (117) Rodina, A.; Dietrich, M.; Göldner, A.; Eckey, L.; Hoffmann, A.; Efros, A.; Rosen, M.; Meyer, B. Free excitons in wurtzite GaN. *Phys. Rev. B* **2001**, *64*, 115204.
- (118) Liang, Y. The substitution modulation on Ca site of CaTiO<sub>3</sub> for transparent conductive oxides from first principles study. *Chem. Phys. Lett.* **2021**, *784*, 139111.
- (119) Kozuka, Y.; Kim, M.; Ohta, H.; Hikita, Y.; Bell, C.; Hwang, H. Enhancing the electron mobility via delta-doping in SrTiO<sub>3</sub>. *Appl. Phys. Lett.* **2010**, *97*, 222115.
- (120) Xie, P.; Yang, F.; Li, R.; Ai, C.; Lin, C.; Lin, S. Improving hydrogen evolution activity of perovskite BaTiO<sub>3</sub> with Mo doping: Experiments and first-principles analysis. *Int. J. Hydrogen Energy* **2019**, *44* (23), 11695–11704.
- (121) Hilal, M.; Rashid, B.; Khan, S. H.; Khan, A. Investigation of electro-optical properties of InSb under the influence of spin-orbit interaction at room temperature. *Mater. Chem. Phys.* **2016**, *184*, 41–48.
- (122) Nishat, S. S.; Hossain, M. J.; Mullick, F. E.; Kabir, A.; Chowdhury, S.; Islam, S.; Hossain, M. Performance Analysis of Perovskite Solar Cells Using DFT-Extracted Parameters of Metal-Doped TiO<sub>2</sub> Electron Transport Layer. *J. Phys. Chem. C* **2021**, *125* (24), 13158–13166.
- (123) Azri, F.; Meftah, A.; Sengouga, N.; Meftah, A. Electron and hole transport layers optimization by numerical simulation of a perovskite solar cell. *Sol. Energy* **2019**, *181*, 372–378.
- (124) Kittel, C. *Introduction to solid state physics*; Wiley, 1966.
- (125) Shen, T.; Hu, C.; Dai, H. L.; Yang, W. L.; Liu, H. C.; Tan, C. L.; Wei, X. L. First principles calculations of magnetic, electronic and

optical properties of (Mn-Fe) co-doped SrTiO<sub>3</sub>. *Optik - International Journal for Light and Electron Optics* **2016**, *127* (5), 3055–3058.

(126) Gillani, S.; Ahmad, R.; Rizwan, M.; Shakil, M.; Rafique, M.; Murtaza, G.; Jin, H. First-principles investigation of structural, electronic, optical and thermal properties of Zinc doped SrTiO<sub>3</sub>. *Optik* **2020**, *201*, 163481.

(127) Aktary, M.; Kamruzzaman, M.; Afrose, R. A comparative study of the mechanical stability, electronic, optical and photocatalytic properties of CsPbX<sub>3</sub> (X = Cl, Br, I) by DFT calculations for optoelectronic applications. *RSC Adv.* **2022**, *12* (36), 23704–23717.

(128) El-Ghtami, H.; Laref, A.; Laref, S. Electronic and optical behaviors of methylammonium and formamidinium lead trihalide perovskite materials. *J. Mater. Sci.: Mater. Electron.* **2019**, *30* (1), 711–720.

(129) Xiong, K.; Robertson, J.; Clark, S. J. Defect states in the high-dielectric-constant gate oxide LaAlO<sub>3</sub>. *Appl. Phys. Lett.* **2006**, *89* (2), 022907.

(130) Dey, A.; Sharma, R.; Dar, S. A.; Wani, I. H. Cubic PbGeO<sub>3</sub> perovskite oxide: A compound with striking electronic, thermoelectric and optical properties, explored using DFT studies. *Comput. Condens. Matter* **2021**, *26*, No. e00532.

(131) Berri, S. Ab initio study of fundamental properties of XAlO<sub>3</sub> (X = Cs, Rb and K) compounds. *J. Sci.* **2018**, *3* (2), 254–261.

(132) Hussain Reshak, A.; Charifi, Z.; Baaziz, H. Ab-initio calculation of structural, electronic, and optical characterizations of the intermetallic trialuminides ScAl<sub>3</sub> compound. *J. Solid State Chem.* **2010**, *183* (6), 1290–1296.

(133) Berri, S. Theoretical analysis of the structural, electronic and optical properties of tetragonal Sr<sub>2</sub>GaSbO<sub>6</sub>. *Chin. J. Phys.* **2017**, *55* (6), 2476–2483.

(134) Copyright *Handbook of Optical Constants of Solids*; Palik, E. D., Ed.; Academic Press, 1998; p iv.

(135) Hayat, S.; Khalil, R. A.; Hussain, M. I.; Rana, A. M.; Hussain, F. A DFT study of perovskite type halides KBeBr<sub>3</sub>, RbBeBr<sub>3</sub>, and CsBeBr<sub>3</sub> in triclinic phase for advanced optoelectronic devices. *Solid State Commun.* **2022**, *344*, 114674.

(136) Mao, Y.; Yao, Z.; Yuan, J.; Chang, X. Two-dimensional germanene-based Janus material Ge<sub>8</sub>HnX<sub>8-n</sub> (n = 0–8, X = F, Cl, Br, I) for photovoltaic and photocatalytic applications. *Appl. Surf. Sci.* **2022**, *598*, 153633.

(137) Dar, S. A.; Sharma, R.; Srivastava, V.; Sakalle, U. K. Investigation on the electronic structure, optical, elastic, mechanical, thermodynamic and thermoelectric properties of wide band gap semiconductor double perovskite Ba<sub>2</sub>InTaO<sub>6</sub>. *RSC Adv.* **2019**, *9* (17), 9522–9532. 10.1039/C9RA00313D

(138) Dey, A. A First-Principles Study of TiX<sub>2</sub> (X = S, Se, and Te) Compounds Optical Properties under the Effect of Externally Applied Electric Field and Strain. *Phys. Solid State* **2020**, *62* (10), 1905–1915.

(139) Pankove, J. I. *Optical processes in semiconductors*; Courier Corporation, 1971; .

(140) Eya, H. I.; Dzade, N. Y. Density Functional Theory Insights into the Structural, Electronic, Optical, Surface, and Band Alignment Properties of BaZrS<sub>3</sub> Chalcogenide Perovskite for Photovoltaics. *ACS Appl. Energy Mater.* **2023**, *6*, S729–S738.

(141) Hofer, F.; Schmidt, F.-P.; Grogger, W.; Kothleitner, G. Fundamentals of electron energy-loss spectroscopy. In *IOP conference series: Materials science and engineering*, 2016; IOP Publishing: Vol. 109, p 012007, .

(142) Arévalo-López, Á. M.; Castillo-Martinez, E.; Alario-Franco, M. A. Electron energy loss spectroscopy in ACrO<sub>3</sub> (A = Ca, Sr and Pb) perovskites. *J. Phys.: Condens. Matter* **2008**, *20* (50), S05207.

(143) Wang, Y.; Djurišić, A. B.; Chen, W.; Liu, F.; Cheng, R.; Feng, S. P.; Ng, A. M. C.; He, Z. Metal oxide charge transport layers in perovskite solar cells—optimizing low temperature processing and improving the interfaces towards low temperature processed, efficient and stable devices. *J. Phys.: Energy* **2020**, *3* (1), 012004.

(144) Feng, R.; Kim, G.; Yu, D.; Chen, Y.; Chen, W.; Liaw, P. K.; An, K. Elastic behavior of binary and ternary refractory multi-principal-element alloys. *Mater. Des.* **2022**, *219*, 110820.

(145) Wang, T.; Wu, C.; Ji, X.; Cui, D. Direct Synthesis of Functional Thermoplastic Elastomer with Excellent Mechanical Properties by Scandium-Catalyzed Copolymerization of Ethylene and Fluorostyrenes. *Angew. Chem.* **2021**, *133* (49), 25939–25944.

(146) Hill, R. The Elastic Behaviour of a Crystalline Aggregate. *Proc. Phys. Soc., London, Sect. A* **1952**, *65* (5), 349–354.

(147) Reuss, A. Berechnung der Fließgrenze von Mischkristallen auf Grund der Plastizitätsbedingung für Einkristalle. *J. Appl. Math. Mech.* **1929**, *9* (1), 49–58.

(148) Voigt, W. *Lehrbuch Der Kristallphysik*; Johnson Reprint Corporation, 1928.

(149) Liu, Y.; Liu, B.; Xiang, H.; Zhou, Y.; Nian, H.; Chen, H.; Yang, G.; Gao, Y. Theoretical investigation of anisotropic mechanical and thermal properties of ABO<sub>3</sub> (A = Sr, Ba; B = Ti, Zr, Hf) perovskites. *J. Am. Ceram. Soc.* **2018**, *101* (8), 3527–3540.

(150) Liu, B.; Wang, J.; Zhou, Y.; Liao, T.; Li, F. Theoretical elastic stiffness, structure stability and thermal conductivity of La<sub>2</sub>Zr<sub>2</sub>O<sub>7</sub> pyrochlore. *Acta Mater.* **2007**, *55*, 2949–2957.

(151) Zhan, X.; Li, Z.; Liu, B.; Wang, J.; Zhou, Y.; Hu, Z. Theoretical Prediction of Elastic Stiffness and Minimum Lattice Thermal Conductivity of Y<sub>3</sub>Al<sub>5</sub>O<sub>12</sub>, YAlO<sub>3</sub> and Y<sub>4</sub>Al<sub>2</sub>O<sub>9</sub>. *J. Am. Ceram. Soc.* **2012**, *95* (4), 1429–1434.

(152) Clarke, D. R. Materials selection guidelines for low thermal conductivity thermal barrier coatings. *Surf. Coat. Technol.* **2003**, *163–164*, 67–74.

(153) Anderson, O. L. A simplified method for calculating the debye temperature from elastic constants. *J. Phys. Chem. Solids* **1963**, *24* (7), 909–917.

(154) Mouhat, F.; Coudert, F.-X. Necessary and sufficient elastic stability conditions in various crystal systems. *Phys. Rev. B: Condens. Matter Mater. Phys.* **2014**, *90* (22), 224104.

(155) Dong, J.; Zhu, H.; Chen, D. Universal elastic-hardening-driven mechanical instability in  $\alpha$ -quartz and quartz homeotypes under pressure. *Sci. Rep.* **2015**, *5* (1), 10810.

(156) Weck, P. F.; Kim, E.; Buck, E. C. On the mechanical stability of uranyl peroxide hydrates: implications for nuclear fuel degradation. *RSC Adv.* **2015**, *5* (96), 79090–79097.

(157) Ayub, S.; Siddique, A.; Khalil, A.; Shaheen, R.; Bilal Tahir, M.; ben hadj hassine, S.; Ullah, Z.; Hannan, A. An extensive investigation of structural, electronic, optical, magnetic, and mechanical properties of YGaO<sub>3</sub> for photovoltaic and optoelectronic applications: First-principles approach. *Inorg. Chem. Commun.* **2023**, *153*, 110754.

(158) Khandy, S. A.; Islam, I.; Gupta, D. C.; Laref, A. Electronic structure, mechanical and thermodynamic properties of BaPaO<sub>3</sub> under pressure. *J. Mol. Model.* **2018**, *24*, 131.

(159) Ugural, A. C.; Fenster, S. K. *Advanced strength and applied elasticity*; Pearson education, 2003.

(160) Yu, X.; Zhou, J.; Liang, H.; Jiang, Z.; Wu, L. Mechanical metamaterials associated with stiffness, rigidity and compressibility: A brief review. *Prog. Mater. Sci.* **2018**, *94*, 114–173.

(161) Razbin, M.; Bagherzadeh, R. Predicting the longitudinal young's modulus of helical auxetic yarn reinforced unidirectional composite. *J. Text. Inst.* **2022**, *114*, 273–281.

(162) Musembi, R.; Mbilo, M. Ab initio study of structural, electronic, elastic, mechanical, and optical properties of K<sub>4</sub>XP<sub>2</sub> (X = Zn, Cd) compounds for optoelectronic applications. *Materialia* **2022**, *26*, 101587.

(163) Hwayyin, R. N.; Ameer, A. S. The Time Dependent Poisson's Ratio of Nonlinear Thermoviscoelastic Behavior of Glass/Polyester Composite. *JJMIE* **2022**, *16* (4), 515–528.

(164) Riaz, M.; Sahar, M. S. U.; Ali, S. M.; Shah, M. F.; Zaidi, S. J.; Khan, M. I. Investigation of stress-induced effects on structural, optoelectronic, and elastic characteristics of cubic CaHfO<sub>3</sub> perovskite oxide; A DFT study. *Comput. Condens. Matter* **2023**, *37*, No. e00846.

(165) Dar, S. A.; Sharma, R.; Mishra, A. K. Phonon stability, electronic structure results, mechanical and thermodynamic properties of RbSbO<sub>3</sub> and CsSbO<sub>3</sub> perovskite oxides: Ab initio investigation. *J. Mol. Graph. Model.* **2019**, *90*, 120–127.

(166) Antonio, J.; Rosas-Huerta, J.; Cervantes, J.; León-Flores, J.; Romero, M.; Carvajal, E.; Escamilla, R. Li/Na atoms' substitution effects on the structural, electronic, and mechanical properties of the CaSnO<sub>3</sub> perovskite for battery applications. *Comput. Mater. Sci.* **2023**, *219*, 112006.

(167) Hasan, M. M.; Kabir, A.; Kamruzzaman, M. The structural, elastic, electronic, magnetic and optical properties of SrNiO<sub>3</sub> perovskite: A DFT and DFT+ U study. *Results Phys.* **2022**, *41*, 105920.

(168) Agne, M. T.; Hanus, R.; Snyder, G. J. Minimum thermal conductivity in the context of diffusion-mediated thermal transport. *Energy Environ. Sci.* **2018**, *11* (3), 609–616.

(169) Pandech, N.; Sarasamak, K.; Limpijumng, S. Elastic properties of perovskite A TiO<sub>3</sub> (A= Be, Mg, Ca, Sr, and Ba) and Pb B O<sub>3</sub> (B= Ti, Zr, and Hf): first principles calculations. *J. Appl. Phys.* **2015**, *117* (17), 174108.